The Astrophysical Journal, 905:171 (15pp), 2020 December 20 https://doi.org/10.3847/1538-4357/abc7c2

The Star-forming Main Sequence and the Contribution of Dust-obscured Star Formation since $z \sim 4$ from the Far-UV+IR Luminosity Functions

Aldo Rodríguez-Puebla[1], Vladimir Avila-Reese[1], Mariana Cano-Díaz[2], S. M. Faber[3], Joel R. Primack[4], José Franco[1], I. Aretxaga[5], and Eder Santiago-Mayoral[1]
[1] Instituto de Astronomía Universidad Nacional Autónoma de México, A.P. 70-264, 04510, México, D.F., Mexico; apuebla@astro.unam.mx
[2] CONACYT Research Fellow—Instituto de Astronomía Universidad Nacional Autónoma de México, A.P. 70-264, 04510, México, D.F., Mexico
[3] UCO/Lick Observatory, Department of Astronomy and Astrophysics, University of California, Santa Cruz, CA 95064, USA
[4] Physics Department, University of California, Santa Cruz, CA 95064, USA
[5] Instituto Nacional de Astrofísica, Óptica y Electrónica (INAOE), Aptdo. Postal 51 y 216, 72000 Puebla, Pue., Mexico
Received 2020 August 11; revised 2020 October 21; accepted 2020 November 3; published 2020 December 28

Abstract

An analytical approach is proposed to study the evolution of the star-forming galaxy (SFG) main sequence (MS) and the fraction of dust-obscured star formation (SF) up to $z \sim 4$. Far-ultraviolet (FUV) and infrared (IR) star formation rates (SFRs) are described as conditional probability functions of M_*. We convolve them with the galaxy stellar mass function (GSMF) of SFGs to derive the FUV and IR luminosity functions (LFs). The two SF modes formalism is used to describe starburst galaxies. By fitting observed FUV and IR LFs, the parameterization of $\mathrm{SFR_{FUV}}-M_*$ and $\mathrm{SFR_{IR}}-M_*$ is constrained. Our derived $\mathrm{SFR_{FUV+IR}}-M_*$ reproduces the evolution of the MS as compared to other observational inferences. At any redshift, we find that the $\mathrm{sSFR_{FUV+IR}}$–M_* relation for MS SFGs approaches a power law at the high-mass end. At lower masses, it bends, and eventually, the slope sign changes from negative to positive at very low masses. At $z \sim 0$, this change of sign is at $M_* \sim 5 \times 10^8\ M_\odot$, close to the dust-obscured SF regime, $M_* \sim 6 \times 10^8\ M_\odot$. The slope sign change is related to the knee of the FUV LF. Our derived dust-obscured fractions agree with previous determinations at $0 \leqslant z \leqslant 2.5$. Dust-obscured fractions depend strongly on mass with almost no dependence on redshift at $z \gtrsim 1.2$. At $z \lesssim 0.75$, high-mass galaxies become more "transparent" compared to their high-redshift counterparts. On the other hand, low- and intermediate-mass galaxies have become more obscured by dust. The joint evolution of the GSMF and the FUV and IR LFs is a promising approach to study mass growth and dust formation/destruction mechanisms.

Unified Astronomy Thesaurus concepts: Galaxy abundances (574); Galaxy counts (588); Galaxy evolution (594); Galaxy processes (614)

1. Introduction

Over the last two decades, major advances have occurred in assembling large galaxy samples from multiwavelength imaging surveys. Now the properties of galaxies are being studied with unprecedented accuracy in statistical representative samples of both local and distant galaxies. This has led to tremendous progress in improving our observational understanding of the evolution of the galaxy stellar mass function (GSMF; for recent discussions and compilations of observations up to high redshifts, see Conselice et al. 2016; Rodríguez-Puebla et al. 2017), as well as the evolution of the star formation rate (SFR) as a function of stellar mass M_* (see, e.g., Daddi et al. 2007; Elbaz et al. 2007; Noeske et al. 2007; Speagle et al. 2014; Rodríguez-Puebla et al. 2017) and the cosmic star formation history (SFH; Madau & Dickinson 2014; Novak et al. 2017; Driver et al. 2018; Liu et al. 2018).

With the above observational advances, the relationship between the SFR and M_* has received intense scrutiny by many authors in recent years. In particular, there is a class of star-forming galaxies (SFGs) that are known to obey a tight SFR–M_* relation, exhibiting $\sim$0.3 dex of scatter and establishing what has been called in the literature the "star-forming main sequence" (MS; Brinchmann et al. 2004; Noeske et al. 2007; Salim et al. 2007; for more recent studies and reviews, see Speagle et al. 2014; Whitaker et al. 2014; Santini et al. 2017). The tightness of this relation and the abundance of galaxies on the MS reflect that most galaxies spend considerable time building their stars in an approximately self-regulated way within this sequence (see, e.g., Bouché et al. 2010; Davé et al. 2012), hence its importance for galaxy formation. Starburst galaxies are another class of SFGs with elevated amounts of star formation, typically associated with galaxy mergers, that are outliers of the MS but represent only a few percent ($\sim$10%–15%) of the total population (Rodighiero et al. 2011; Sargent et al. 2012). Quenched galaxies are another class of galaxies that are off the MS, in this case due their low levels of star formation (e.g., Wuyts et al. 2007; Williams et al. 2009); their fraction has increased rapidly since $z \lesssim 2$ (Muzzin et al. 2013). In this paper, we focus on MS SFGs.

Considering these now well-established findings, there are still some open questions with respect to the distribution of the SFRs of SFGs. Does the SFR–M_* relationship extend to low-mass galaxies and dwarfs, $M_* \lesssim 10^9\ M_\odot$, with the same slope as intermediate- and high-mass galaxies? What is the contribution from dust-obscured star formation as a function of stellar mass and redshift?

This paper addresses the above questions by using the redshift evolution of the far-ultraviolet (FUV; 1500 Å) and total infrared (IR; 8–1000 μm) rest-frame luminosity functions (LFs) combined with the evolution of the GSMFs of SFGs. The above questions have been studied separately by some authors in the past; for example, Kurczynski et al. (2016), McGaugh et al. (2017), Iyer et al. (2018), and Davies et al. (2019) studied the SFR–M_* relation at low masses, while Pannella et al. (2009) and Whitaker et al. (2017) studied the contributions from dust-obscured star formation. Normally, the approach

employed by these and other authors is to determine those properties galaxy-by-galaxy from galaxy samples. However, the galaxy-by-galaxy approach fails to check the consistency with other important statistical quantities that provide valuable constraints, such as the GSMF and the FUV and IR LFs. Thus, it is key that robust determinations of the total SFRs and the portions associated with the unobscured, SFR_{FUV}, and obscured, SFR_{IR}, regimes must be consistent with the GSMF and the FUV and IR LFs. Specifically, it is important and timely to address the above two questions at the same time, as well as their possible physical correlations and implications for galaxy formation models in light of the joint evolution of the GSMF and the FUV and IR LFs. Moreover, we note that the joint evolution of the GSMF and the FUV and IR rest-frame LFs has not yet received attention in light of the above questions. To our knowledge, there is only one study that exploits the joint evolution of the GSMF and the FUV and IR LFs: Bernhard et al. (2014). In that paper, the authors developed a phenomenological approach to estimate the FUV and IR LFs based on the observed GSMF, the SFR–M_* relationship, and the dust attenuation, IRX. Although here we revolve around a similar idea, our goal is different.[6]

Our main goal for this paper is to exploit the power of using the joint evolution of the GSMF and the FUV and IR LFs as an alternative way to derive and study the SFR–M_* relationship and its decomposition into the unobscured and obscured contributions. Thus, our approach exploits data not previously used to derive the SFR–M_* relationship for MS SFGs. This is independent of the galaxy-by-galaxy approach, which is based on galaxy surveys that could be subject to biases and incompleteness. One of the main findings of this paper is that our results are in agreement with the galaxy-by-galaxy approach, providing the kind of end-to-end test needed to verify the consistency between the SFRs, including their unobscured and obscured contributions, and the GSMF and the FUV and IR LFs. We also find that the joint evolution of the GSMF and the FUV and IR LFs offers a powerful tool that contributes to the study of the emergence of the galaxy mass distributions, stellar mass growth, and dust formation/destruction and ultimately better constrains the galaxy formation models.

This paper is divided into four sections. The analytical method we employed to link M_* to SFR is introduced in Section 2. Section 3 presents our results and compares to a set of independent observations, finding a good agreement between them. Our approach represents a new powerful and novel tool to study the redshift evolution of MS SFGs and the dependence of the fraction of dust-obscured star formation with stellar mass at the same time. Finally, in Section 4, we summarize and discuss our results.

In this paper, we adopt the following cosmological parameter values: $\Omega_\Lambda = 0.7$, $\Omega_m = 0.3$, and $h = 0.7$. All stellar masses are normalized to a Chabrier (2003) initial mass function (IMF).

[6] There are, however, other notable studies that have combined some but not all of them at the same time. For example, Béthermin et al. (2012) used the IR LF and the GSMF, while Burgarella et al. (2013) used the FUV and IR. More recently, Tacchella et al. (2018) used the FUV to study the distribution of SFRs.

2. Modeling the FUV+IR SFR Distributions

Here we present a mathematical approach to derive the redshift evolution of the conditional distribution of SFR given M_* for MS galaxies and all its moments. In particular, our main aim is the derivation of the redshift evolution of the mean SFR–M_* relationship for MS galaxies. Normally, the evolution of the MS is inferred by combining galaxy samples at different redshifts for which the SFRs are estimated for every galaxy (e.g., Whitaker et al. 2014; Salim et al. 2016). At this point, it should be said that (i) galaxy samples are subject to (their own) selection effects, and (ii) the SFRs reported by different authors are based on different tracers and methods. As a result, the derived SFR–M_* relation and its evolution will be biased. On the other hand, the comparison of the SFR–M_* relation and its evolution estimated in different ways is not trivial, though some authors have attempted to homogenize different determinations (see, e.g., Speagle et al. 2014; Rodríguez-Puebla et al. 2017). Thus, to infer robust relations, especially for accurately constraining the shape of the MS in broad mass and redshift ranges, it is optimal to use a homogeneous method to calculate the SFRs from galaxy samples for which the volume completeness is well defined. This is the approach used here.

As mentioned earlier, the novelty of our approach is that it combines observational FUV and IR rest-frame LFs at different redshifts with the GSMFs of SFGs to derive the mean SFR–M_* relationship and its scatter over broad mass and redshift ranges. The advantage of this approach is that it has a uniform way to determine the SFRs at all redshifts, and the sample completeness above given limits is well controlled.

In the following, we describe how we constrain the conditional distribution of SFRs given M_* when combining the FUV and IR LFs and the GSMFs of SFGs at different redshifts. Use of conditional distributions allows us to compute any moment, in particular the first moment, that is, the mean SFR–M_* relationship. Notice that our method naturally separates the SFRs into their unobscured and dust-obscured components, allowing study of the dust-obscured fraction at the same time.

2.1. The FUV and IR Conditional SFR Distributions

Motivated by observations, we assume that the MS is a nondecreasing relation between M_* and SFR. The key assumption in our approach is that the FUV and IR SFR conditional probability distributions as a function of M_* convolved with the observed GSMFs of SFGs gives the FUV and IR rest-frame LFs. In other words, we are assuming that the FUV and IR LFs emerged from the MS galaxy population. This is actually inaccurate in the case of the IR LF, as starburst galaxies also contribute to the LF (see, e.g., Sargent et al. 2012; Gruppioni et al. 2013). Fortunately, their contribution becomes relatively important only at the high-luminosity end, and this can be estimated. Following the results presented in Sargent et al. (2012), we assume that the IR-based SFR distribution is composed of the contributions of both MS and starburst galaxies; this is known in the literature as two star formation modes formalism. Next, we will discuss the conditional SFR distributions given M_* and their moments. While all of the quantities that we discuss below depend on redshift, we do not show this dependence for simplicity.

We begin by introducing the mean $\langle \log SFR_{FUV}(M_*) \rangle$ and $\langle \log SFR_{IR}(M_*) \rangle$ relations and our proposed parametric

functions. To our knowledge, there are no parametric functions previously reported in the literature for these relations. We propose our parametric functions by noticing that the generic shapes of the $\mathrm{SFR_{FUV}}$–M_* and $\mathrm{SFR_{IR}}$–M_* relations are governed by the shape of their corresponding FUV and IR LFs. For the mean $\mathrm{SFR_{FUV}}$–M_* relation, we assume a double power law (defined by four parameters: $\mu_{\mathrm{FUV},0}$, α, β, and M'_{FUV}),

$$\langle \log \mathrm{SFR_{FUV}}(M_*)\rangle = \mu_{\mathrm{FUV},0} + \log\left(\frac{2}{\left(\frac{M_*}{M'_{\mathrm{FUV}}}\right)^{\alpha} + \left(\frac{M_*}{M'_{\mathrm{FUV}}}\right)^{\beta}}\right), \quad (1)$$

while for the mean $\mathrm{SFR_{IR}}$–M_*, we assume a Gompertz-like function that dominates at the low-mass end and a power law that dominates at the high-mass end (defined by three parameters: $\mu_{\mathrm{IR},0}$, γ, and M'_{IR}):

$$\langle \log \mathrm{SFR_{IR}}(M_*)\rangle = \mu_{\mathrm{IR},0} + \log\left(\frac{(M_*/M'_{\mathrm{IR}})^{\gamma}}{\exp(-e^{-\log(M_*/M'_{\mathrm{IR}})})}\right). \quad (2)$$

As mentioned above, all of the parameters from the above equations depend on redshift. In Section 2.3, we discuss the functions that we use for the dependences with redshift and their corresponding best-fitting parameters to the observational data through our approach.

To describe the conditional SFR distributions, we introduce the conditional lognormal distribution $\mathcal{N}(y|x)$, given by

$$\mathcal{N}(y|x)d\log y = \frac{d\log y}{\sqrt{2\pi\sigma_y^2}}\exp\left[-\frac{(\log y - \mu(x))^2}{2\sigma_y^2}\right], \quad (3)$$

where the mean is $\mu(x) = \langle \log y(x)\rangle$, and σ_y is the logarithmic width of the distribution, i.e., its scatter. Since we will work in a space in which the logarithm of y is lognormally distributed, for simplicity, we will sometimes refer to $\langle \log y(x)\rangle$ as the mean y–x relation. In some cases, authors reported $\langle y\rangle$; for a lognormal distribution, the offset between $\langle \log y\rangle$ and $\langle y\rangle$ is given by (see, e.g., Rodríguez-Puebla et al. 2017)

$$\log\langle y\rangle = \langle \log y\rangle + \frac{\sigma^2}{2}\ln 10. \quad (4)$$

We define the conditional probability distribution of SFRs given a stellar mass as $\mathcal{P}_{\mathrm{SFR},X}(\mathrm{SFR}_X|M_*)$, where X refers to the SFRs computed based on the FUV or IR rest-frame luminosities. In the case of $\mathrm{SFR_{FUV}}$, we assume that $\mathcal{P}_{\mathrm{SFR,FUV}} = \mathcal{N}(\mu_{\mathrm{FUV}}, \sigma_{\mathrm{FUV}})$ with a scatter σ_{FUV} independent of M_* and mean $\mu_{\mathrm{FUV}} = \langle \log \mathrm{SFR_{FUV}}(M_*)\rangle$, given by Equation (1). As for the distribution of $\mathrm{SFR_{IR}}$, as mentioned above, it is composed of the contributions of MS and starburst galaxies. Therefore,

$$\mathcal{P}_{\mathrm{SFR,IR}} = (1 - \mathcal{A}_{\mathrm{SB}}) \times \mathcal{P}_{\mathrm{SFR,IR-MS}} + \mathcal{A}_{\mathrm{SB}} \times \mathcal{P}_{\mathrm{SFR,IR-SB}},$$

where $\mathcal{A}_{\mathrm{SB}}$ is the fraction of starburst galaxies at fixed stellar mass, and the conditional distributions $\mathcal{P}_{\mathrm{SFR,IR-MS}}$ and $\mathcal{P}_{\mathrm{SFR,IR-SB}}$ are lognormally distributed (Equation (3)). Following Sargent et al. (2012), we assume that $\sigma_{\mathrm{IR}}(= \sigma_{\mathrm{IR-SB}} = \sigma_{\mathrm{IR-MS}})$ and $\mathcal{A}_{\mathrm{SB}}$ are both independent of mass and that $\mu_{\mathrm{IR-SB}} = \mu_{\mathrm{IR-MS}} + \Delta\mu_0$, where $\mu_{\mathrm{IR-MS}} = \langle \log \mathrm{SFR_{IR-MS}}(M_*)\rangle$ is the mean relation for the MS galaxies (give by Equation (2); hereafter, we will refer to it just as $\langle \log \mathrm{SFR_{IR}}\rangle$). Based on the recent results from Schreiber et al. (2015), we use $\mathcal{A}_{\mathrm{SB}} = 0.033$ and $\Delta\mu_0 = 0.79$ dex.[7]

As for the scatters σ_{FUV} and σ_{IR}, first note that observations based on mass-complete samples have shown that the scatter around the SFR–M_* relationship is of the order of 0.3 dex (Speagle et al. 2014; Schreiber et al. 2015; Cano-Díaz et al. 2016; Fang et al. 2018). Nonetheless, recent results have shown that the scatter could increase up to ∼0.4 dex at the high-mass end (Ilbert et al. 2015; Popesso et al. 2019b, 2019a). While the discussion of the real trends and values of the MS scatter is beyond the scope of this paper, here we assume a constant scatter of $\sigma_{\mathrm{FUV}} = 0.3$ dex for the FUV and $\sigma_{\mathrm{IR}} = 0.4$ for the IR and, for simplicity, zero covariance between the two distributions. The above will lead to a scatter around the inferred mean SFR–M_* relations that has some dependence on M_* (see Equation (17) described below) in the direction that for low-mass galaxies, $\sigma \sim 0.3$ dex, while for massive galaxies, $\sigma \sim 0.4$ dex.

2.2. The FUV and IR LFs

In this section, we describe how the FUV and IR LFs are derived by convolving the GSMFs of SFGs and the conditional FUV and IR SFR probability distributions. For the above, we begin by using the Kennicutt (1998) conversion factors, $\mathcal{K}_X$, to transform SFRs into luminosities, that is, $L_X = \mathcal{K}_X/\mathrm{SFR}_X$. These conversion factors allow us to pass from the SFR conditional probability distributions, $\mathcal{P}_{\mathrm{SFR},X}(\mathrm{SFR}_X|M_*)$, to the respective distributions of luminosities, $\mathcal{P}_{l,X}(L_X|M_*)$. Then, the LF of the FUV and IR light is related to the GSMFs of SFGs, $\phi_{*,\mathrm{SF}}$, by the following convolution:

$$\phi_X(L_X) = \int \mathcal{P}_{l,X}(L_X|M_*)\,\phi_{*,\mathrm{SF}}(M_*)\,d\log M_*. \quad (5)$$

For the GSMFs of SFGs, we use the best-fitting model for the compiled GSMF data from Rodríguez-Puebla et al. (2017) and their reported evolution of the fraction of SFGs as a function of M_* (for details, see Appendix). We note that the above integral is not computed from $M_* = 0$ but from $M_* = 10^6\ M_\odot$, which is still ∼1–1.5 dex below the observational limit of our GSMFs.

The observational LFs are actually reported over redshift intervals $z_i < z < z_f$. We take the above into account by using the following equation:

$$\phi_{\mathrm{obs},X}(L_X; z_i, z_f) = \frac{\int_{z_i}^{z_f}\phi_X(L_X, z)dV}{V(z_f) - V(z_i)}, \quad (6)$$

where V is the comoving volume.

[7] Note that this value slightly differs from the one reported in Schreiber et al. (2015). The reason for this is that we are taking into account that the distribution between the ratio of the specific star formation rates (sSFRs) and the mean sSFR from the MS (R_{SB}, the starburstiness parameter defined by the authors) is not centered on $R_{\mathrm{SB}} = 1$; see their best-fit models for their Equation (10) and Figure 19.

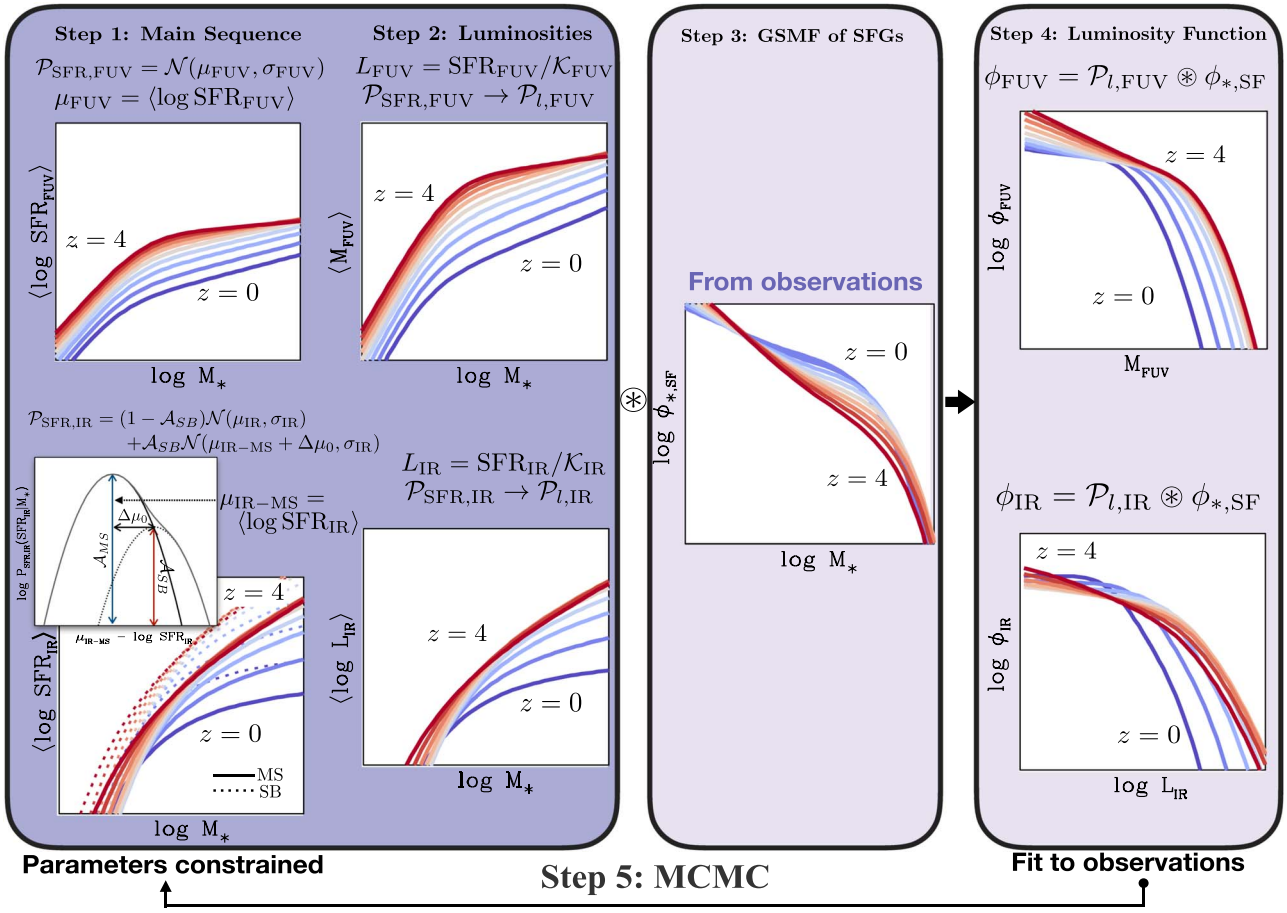

Figure 1. Scheme with the steps to constrain the means of SFR given M_* at different redshifts from fitting the observational FUV and IR LFs and knowing the GSMFs of SFGs; see text for details.

The original Kennicutt (1998) conversion factors were obtained on the assumption of a Salpeter (1955) IMF.[8] According to Madau & Dickinson (2014), we multiply the original conversion factors by 0.63 to convert them into a Chabrier (2003) IMF; the FUV conversion factor changes to $\mathcal{K}_{\rm FUV} = 1.7 \times 10^{-10} M_\odot$ yr^{-1} $L_\odot^{-1}$, while the IR factor changes to $\mathcal{K}_{\rm IR} = 1.09 \times 10^{-10} M_\odot$ yr^{-1} $L_\odot^{-1}$. Notice that the FUV light refers to the observed luminosity, which can be obscured in the presence of dust. In the following, we assume that the fraction of FUV light emitted by young stars that is absorbed by dust is directly proportional to the fraction that is reemitted in the IR (wavelength range 8–1000 μm), as is often assumed in the literature (da Cunha et al. 2008).

2.3. Constraining the FUV+IR SFR Distributions

Under the assumption of a monotonic increasing relation between L_X (X = FUV or IR) and M_*, Equation (5) shows how this relation or, more generally, the respective luminosity conditional probability distribution maps the GSMFs of SFGs into the FUV or IR LF. These FUV and IR luminosity distributions are tracers of the respective SFR distributions. Our next aim is to self-consistently constrain these SFR distributions (FUV, IR, and the total) from the observations. Figure 1 summarizes the steps described in the previous subsections and here. The steps are as follows.

1. *Step 1.* Define the FUV SFR conditional probability distribution $\mathcal{P}_{\rm SFR,FUV}$ as a lognormal function. Use the two-star formation mode from Sargent et al. (2012) to separate the contribution from MS and starburst galaxies. Define the IR SFR conditional probability distribution as $\mathcal{P}_{\rm SFR,IR} = (1 - \mathcal{A}_{\rm SB})\mathcal{P}_{\rm SFR,IR-SF} + \mathcal{A}_{\rm SB}\mathcal{P}_{\rm SFR,IR-SB}$. Both $\mathcal{P}_{\rm SFR,IR-SF}$ and $\mathcal{P}_{\rm SFR,IR-SB}$ are assumed to be lognormal functions. Propose redshift-dependent parametric functions for the mean relations $\langle \log {\rm SFR}_{\rm FUV}(M_*)\rangle$ and $\langle \log {\rm SFR}_{\rm IR}(M_*)\rangle$, Equations (1) and (2), respectively.
2. *Step 2.* Convert SFRs into luminosities using the Kennicutt (1998) conversion factors. This allows us to pass from the conditional distributions $\mathcal{P}_{\rm SFR,FUV}$ and $\mathcal{P}_{\rm SFR,IR}$ to the conditional distributions $\mathcal{P}_{l,\rm FUV}$ and $\mathcal{P}_{l,\rm IR}$, respectively.
3. *Step 3.* Characterize the redshift evolution of the observational GSMFs of SFGs, $\phi_{*,\rm SF}$. Appendix presents our best-fitting model for the compiled GSMFs and the fraction of SFGs as a function of redshift from Rodríguez-Puebla et al. (2017).

[8] Using the conversion factors is a very popular approach to empirically relate SFRs to luminosities. While there is some justification in using this method, it may nevertheless yield values that are different from the real ones. For example, the conversion factor of the SFR diagnostic based on the FUV light depends on the metal enrichment and SFH of a galaxy. This could lead to differences up to ~0.5 dex in the conversion factor when exploring different combinations of these dependencies (see Figure 3 from Madau & Dickinson 2014; see also Tacchella et al. 2018). While the above introduces an uncertainty that could be taken into account in our analysis, we decided to use the most popular calibration factors from the literature because this facilitates the comparison with previous works. Therefore, we do not consider more complex conversion factors that depend on metallicity and SFHs.

4. *Step 4.* Derive the FUV and IR LFs by convolving the GSMFs of SFGs with their corresponding conditional luminosity distributions (Equation (5)): $\phi_{\rm FUV} = \mathcal{P}_{l,\rm FUV} \circledast \phi_{*,\rm SF}$ and $\phi_{\rm IR} = \mathcal{P}_{l,\rm IR} \circledast \phi_{*,\rm SF}$.
5. *Step 5.* Adjust the redshift-dependent parameters of the mean $\langle \log {\rm SFR}_{\rm FUV}(M_*)\rangle$ and $\langle \log {\rm SFR}_{\rm IR}(M_*)\rangle$ relations. This is possible because steps 1–4 relate the mean relations to the observed FUV and IR LFs.

Next, we describe the parameterization and best-fitting model of the redshift evolution of the mean ${\rm SFR}_{\rm FUV}$–M_* and ${\rm SFR}_{\rm IR}$–M_* relations.

Each of the parameters described by Equations (1) and (2) depends on redshift. After some experimentation, we found that the redshift z dependence of these parameters is well described by the following function composed of three free parameters:

$$\mathcal{Q}(q_1, q_2, q_3, z) = q_1 + q_2 \log(1+z) + q_3 z^2. \quad (7)$$

In this paper, we find the best-fitting parameters by using a Bayesian approach through a Markov Chain Monte Carlo method applied jointly to the data following Rodríguez-Puebla et al. (2013).

Figure 2 shows a compilation of measured rest-frame FUV LFs between $z = 0$ and 9 from 21 observational studies that are listed in Table 1. The FUV LFs were not corrected for dust attenuation but homogenized to our adopted cosmology. We use this compilation to find the best-fit parameters to the evolution of the mean ${\rm SFR}_{\rm FUV}$–M_* relationship. The solid lines in Figure 2 show our best-fitting model for the LF $\phi_{\rm obs,FUV}$. The best-fit parameters of the redshift-dependent mean ${\rm SFR}_{\rm FUV}$–M_* relationship are

$$\mu_{\rm FUV,0}(z) = \mathcal{Q}(-1.451 \pm 0.011, 2.471 \pm 0.027, -0.001 \pm 0.0004, z), \quad (8)$$

$$\log M_{\rm FUV}(z) = \mathcal{Q}(8.343 \pm 0.011, 0.705 \pm 0.030, 0.002 \pm 0.0007, z), \quad (9)$$

$$\alpha(z) = \mathcal{Q}(-0.543 \pm 0.009, 1.978 \times 10^{-5} \pm 0.002, 0.010 \pm 0.0002, z), \quad (10)$$

$$\beta(z) = \mathcal{Q}(0.667 \pm 0.006, 0.033 \pm 0.015, 0.012 \pm 0.0004, z). \quad (11)$$

The observed IR LFs from $z = 0$ to 4.2 are shown in Figure 3 from a compilation of eight observational studies listed in Table 2. Similarly, the data above were homogenized to our adopted cosmology. Using these data, as in the case of the FUV data, we constrain the best-fit parameters of the redshift-dependent mean ${\rm SFR}_{\rm IR}$–M_* relationship:

$$\mu_{\rm IR,0}(z) = \mathcal{Q}(0.127 \pm 0.017, 5 \pm 0.044, -0.168 \pm 0.028, z), \quad (12)$$

$$\log M_{\rm IR}(z) = \mathcal{Q}(9.850 \pm 0.031, 1.876 \pm 0.087, -0.107 \pm 0.030, z), \quad (13)$$

$$\gamma(z) = \mathcal{Q}(0.051 \pm 0.011, 0.983 \pm 0.066, 0, z). \quad (14)$$

Our best-fitting model is shown with the red solid lines in Figure 3.

2.4. The Total SFR Distribution: The Mean SFR–M_* Relation and the Scatter

Once the redshift-dependent parameters of the mean $\langle \log {\rm SFR}_{\rm FUV}(M_*)\rangle$ and $\langle \log {\rm SFR}_{\rm IR}(M_*)\rangle$ relations are constrained, we compute the total (FUV+IR) SFR–M_* relation and the scatter around it. Thus, the final step in our program is to characterize the total conditional SFR distribution at a fixed M_* for galaxies from the FUV- and IR-based conditional SFR distributions. Formally, the total SFR distribution is given by

$$\mathcal{P}_{\rm SFR}({\rm SFR}|{\rm M}_*) = \int \frac{\mathcal{P}_{\rm SFR,FUV}({\rm SFR} - {\rm SFR}_{\rm IR}|{\rm M}_*)}{1 - {\rm SFR}_{\rm IR}/{\rm SFR}} \times \mathcal{P}_{\rm SFR,IR-MS}({\rm SFR}_{\rm IR}|M_*) d\log {\rm SFR}_{\rm IR}. \quad (15)$$

Note that for the IR SFR distribution, we use only the component of MS galaxies.

A few words on the above distribution are worth mentioning at this point. While the sum of normally distributed random variables is also normally distributed, this is not the case for lognormally distributed random variables. To our knowledge, there is no analytical solution for lognormal distributions, so this is computed numerically via Equation (15). From the above equation, we can derive the total mean (hereafter, we will sometimes refer to it simply as the mean) SFR–M_* relation:

$$\langle \log {\rm SFR}(M_*)\rangle = \int \log {\rm SFR} \mathcal{P}_{\rm SFR}({\rm SFR}|M_*) d\log {\rm SFR}. \quad (16)$$

The scatter around the mean is

$$\sigma^2_{\rm SFR}(M_*) = \int (\log {\rm SFR} - \langle \log {\rm SFR}(M_*)\rangle)^2 \times \mathcal{P}_{\rm SFR}({\rm SFR}|M_*) d\log {\rm SFR}. \quad (17)$$

We will also report the mean $\langle \log {\rm sSFR}(M_*)\rangle$ relation with ${\rm sSFR} = {\rm SFR}/M_*$ and $\sigma_{\rm sSFR} = \sigma_{\rm SFR}$. Since we separately use the observations of the IR and FUV LFs, a straightforward outcome of our approach is the determination of the separate contributions from the FUV and IR to the total SFRs. This will be important for deriving the dust-obscured fraction as a function of mass and redshift.

3. Results

Before discussing our results, we note that the observed IR LF is the main source of uncertainty in the conclusions that will be presented below. This is due to its restricted redshift, $z \lesssim 4$, and luminosity range; see Figure 3. This is not the case for the FUV LF and the GSMF, which are available up to $z \sim 9$ and cover several orders of magnitude from low- to high-luminosity/mass galaxies; see Figure 2 and also Figure 11 from Appendix. In order to reduce the risk of overinterpreting our results, in the figures below, we will explicitly indicate the regimes over which our IR LFs are valid (the exception will be Figure 9, but this is discussed in the text).

In Figure 4, we present our resulting $\langle \log {\rm SFR}\rangle$ (see Equation (16)) as a function of redshift for five stellar mass bins. The solid lines indicate the stellar mass ranges where the best-fitting models of both the FUV and IR LFs are constrained by the data. The dashed lines indicate the range over which the IR LFs have been extrapolated but there are observational data to constrain the best-fit models of the FUV LF. The shaded area shows the scatter around the mean relation using Equation (17). Note that the above limitation in the data affects mostly low-mass galaxies, $M_* \lesssim 10^9\ M_\odot$.

Figure 4 compares our results to several observational studies listed in Table 3 for galaxies with masses above $M_* \sim 0.5{-}1 \times 10^9\ M_\odot$. The compiled data have been homogenized to the same

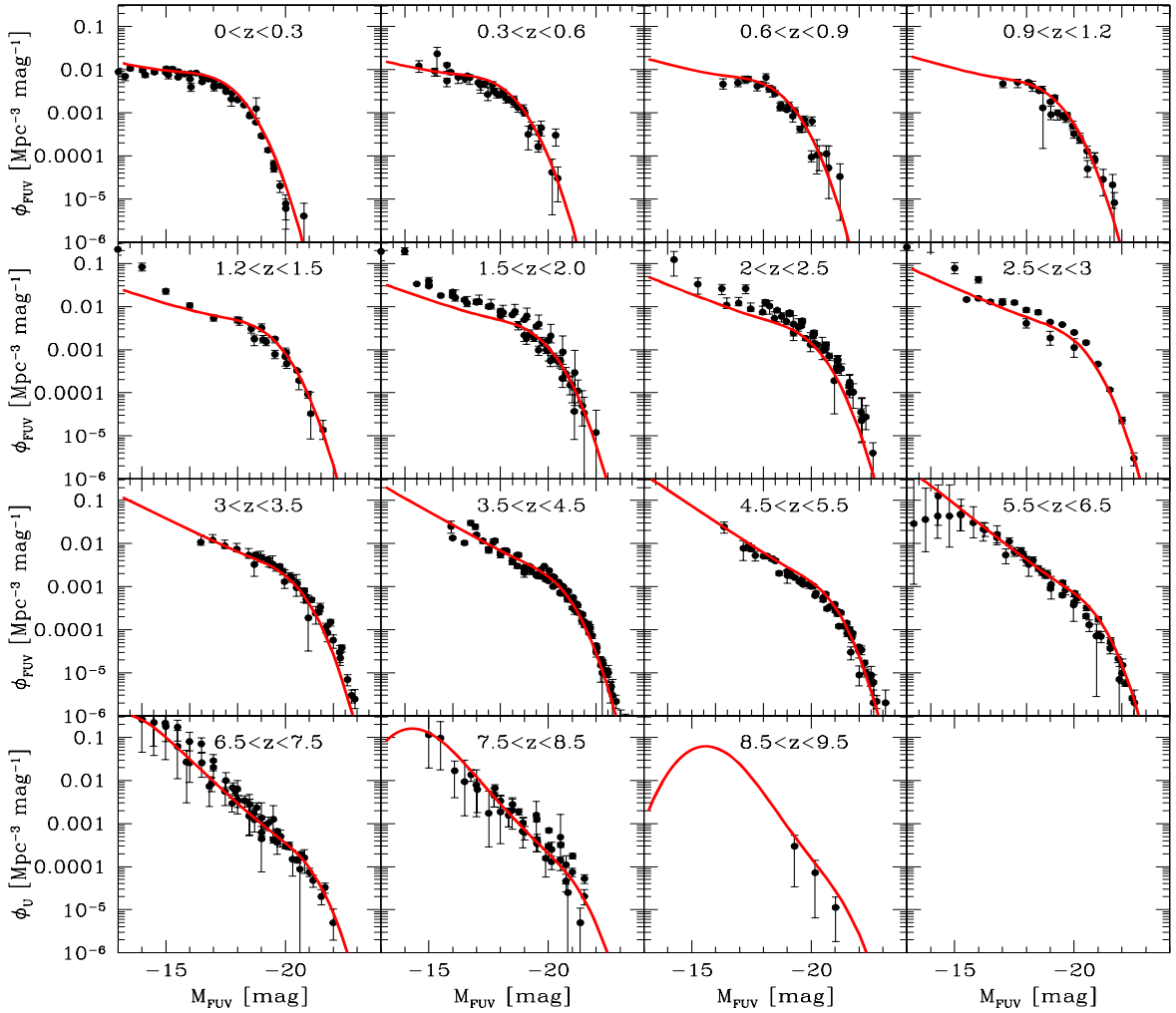

Figure 2. The FUV LF. The red solid lines present the best-fitting models for a compilation of 21 observational studies; see Table 1. The data have been homogenized to the same cosmology. The turnover at the faint end at $z > 7.5$ is due to the lower limit of M_* considered for the integral in Equation (5).

Table 1
FUV LFs

Author	Redshift
Cucciati et al. (2012)	$0.05 < z < 4.5$
Arnouts et al. (2005)	$0.055 < z < 3.5$
Driver et al. (2012)	$0.013 < z < 0.1$
Robotham & Driver (2011)	$0.013 < z < 0.1$
Oesch et al. (2010)	$0.75 \lesssim z \lesssim 2.5$
Alavi et al. (2016)	$1 < z < 3$
Hathi et al. (2010)	$1 < z < 3$
Mehta et al. (2017)	$1.4 < z < 3.6$
Reddy & Steidel (2009)	$1.9 < z < 3.4$
Alavi et al. (2014)	$z \sim 2$
Parsa et al. (2016)	$2 < z < 4$
van der Burg et al. (2010)	$3 < z < 5$
Ono et al. (2018)	$4 < z < 7$
Bouwens et al. (2007)	$4 \lesssim z \lesssim 5$
Finkelstein et al. (2015)	$4 \lesssim z \lesssim 8$
Bouwens et al. (2015)	$4 \lesssim z \lesssim 8$
Atek et al. (2018)	$z \sim 6$
Livermore et al. (2017)	$6 < z < 8$
Bhatawdekar et al. (2019)	$6 < z < 9$
Bouwens et al. (2011)	$7 \lesssim z \lesssim 8$
Oesch et al. (2012)	$z \sim 8$

Chabrier (2003) IMF. In addition, in cases where the authors reported the mean ⟨SFR⟩, we use Equation (4) to transform it into the mean ⟨logSFR⟩. We also compute the mean SFR–M_* relationship at $z \sim 0$ for Sloan Digital Sky Survey (SDSS) galaxies using the GALEX–SDSS–WISE Legacy Catalog (GSWLC; Salim et al. 2016, 2018). Here we use the deep GSWLC-2 catalog based on UV, optical, and 22 μm data from the Wide-field Infrared Survey Explorer (WISE) to derive SFRs using spectral energy distribution (SED) fitting techniques; for details, see Salim et al. (2018). From this catalog, we use the derived SFRs, based on both the UV and IR components, to compute the average SFR–M_* for MS SFGs as described next. First, we note that we use a slightly modified version of the SFR–M_* relation by Speagle et al. (2014) adapted for the GSWLC-2 catalog. Then, galaxies −0.7 dex ($\sim 2.3\sigma$) away from the ridgeline are excluded. Next, we performed a power-law fit to the MS for the trimmed sample and again galaxies −0.7 dex away from the ridgeline were excluded. We repeated the above processes three more times. We note that on the last iteration, the parameters of the power-law fits did not change considerably. This is similar to what has been proposed in Fang et al. (2018) in order to obtain relations that are close to the highest-density ridgeline of the MS. In Figure 4, the colors indicate the different calibrators reported by the authors. Note, however,

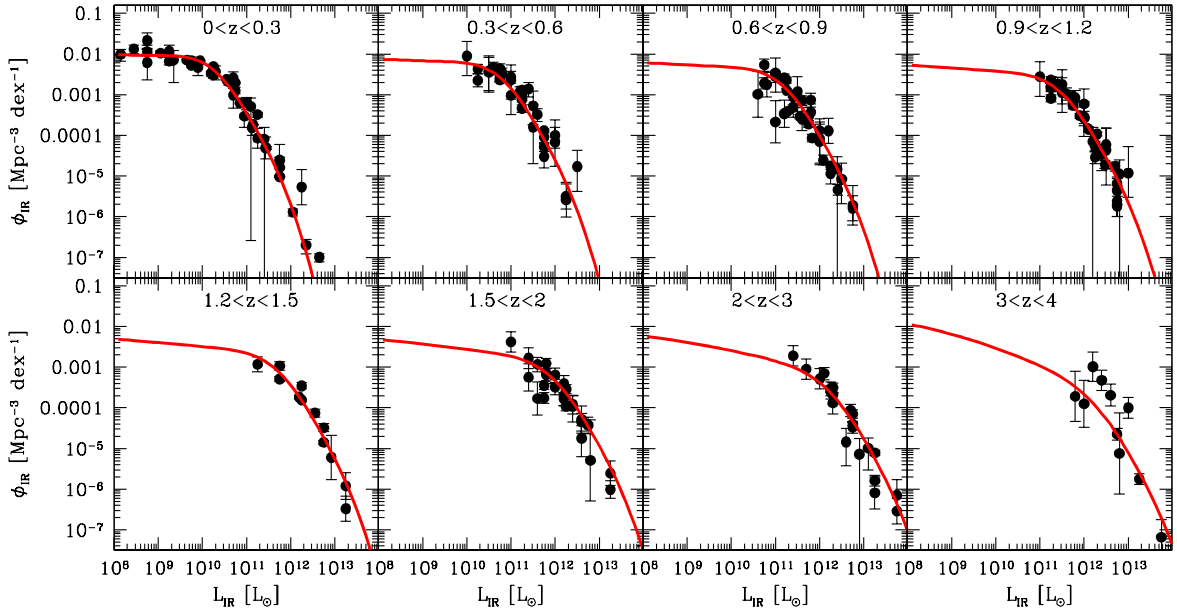

Figure 3. The IR LF. Solid lines present the best fit from a compilation of eight observational studies; see Table 2. Similar to the FUV LFs, the data have been homogenized to the same cosmology.

Table 2
IR LFs

Author	Redshift
Kilerci Eser & Goto (2018)	$0 < z < 0.3$
Le Floc'h et al. (2005)	$0 < z < 1$
Casey et al. (2012)	$0 < z < 1.6$
Rodighiero et al. (2010)	$0 < z < 2.5$
Lim et al. (2020)	$0 < z < 4$
Gruppioni et al. (2013)	$0 < z < 4.2$
Magnelli et al. (2013)	$0.1 < z < 2.3$
Magnelli et al. (2011)	$1.3 < z < 2.3$

that most of the data compiled in this paper are based on FUV+IR measurements for a more direct comparison to our results.

In excellent agreement with the set of independent observations from Table 3, our results reproduce both the strong evolution of the SFR with z and the dependence on M_*. Even when we have extrapolated our best fits to the IR LFs, as indicated by the dashed lines in Figure 4, our results are consistent with the set of observations from Table 3. We emphasize that we did not fit to these data, but our results fell out naturally from the joint fit to the LFs and the GSMF.

Figure 5 shows the obtained sSFR–M_* relation for MS galaxies from $z \sim 0$ to 4. Here our results are again consistent with the compiled data. The consistency presented in Figures 4 and 5 is not trivial, since the compilation described above is composed of measurements based on different surveys and calibrators (though most are based on FUV+IR measurements). We thus conclude that our derived SFRs describe quite well a set of independent observational inferences over the range where both the IR and FUV LFs are available. A straightforward implication from the above is that the joint evolution of the GMSF and the FUV and IR LFs is self-consistent; that is, the evolution of the FUV+IR SFR of MS galaxies is consistent with their stellar mass growth. The reason for this is that in our approach, the FUV+IR LF is the result of convolving the GSMF of SFGs with the SFR conditional distribution given M_*; see Equation (6) and Figure 1.

We notice that our derived sSFR–M_* relations at all redshifts are not well described by simple power laws. A curvature in the MS has already been documented in previous works (see, e.g., Whitaker et al. 2014; Gavazzi et al. 2015; Lee et al. 2015; Schreiber et al. 2015; Tomczak et al. 2016; Lee et al. 2018; Popesso et al. 2019a; Leslie et al. 2020). In general, our MS at any z follows a power law only at the high-mass end, with the mass at which the relation departs from the power law decreasing with z roughly from $M_* \sim 10^{11}$ at $z > 2$ to $M_* \sim 2 \times 10^{10}$ at $\sim$0. The slope at $z \sim 0$ for galaxies above $M_* \sim 10^{10}\ M_\odot$ is ~ -0.71. At lower masses and at any redshift, the MS bends until an inflection point is attained. In the sSFR–M_* plane, this means that the MS changes sign. At $z \sim 0$, we find that at low masses, $M_* \lesssim 10^{8.8}\ M_\odot$, the slope is $\sim$0.37, while for $M_* \sim 10^9$–$10^{10}\ M_\odot$, the slope is $\sim$0.37. This is an interesting feature of the MS at low masses that our method has allowed us to establish. In the following, we discuss it in more detail.

3.1. The MS of Low-mass and Dwarf Galaxies

Next, we explore our results for low-mass galaxies, $10^8 \lesssim M_*/M_\odot \lesssim 10^9$. Our low-mass limits are restricted by the observational availability of both the FUV and IR LFs. This affects the robustness of our derivations at masses below $M_* \sim 5 \times 10^9\ M_\odot$, in particular for redshifts larger than $z \sim 0.5$. For low-mass galaxies, our results are based mainly on the FUV LFs and, to a lesser extent, on the extrapolations of the IR LFs, due to the flat faint-end slopes of the latter (see Figure 3). It is thus important to understand the robustness of our inferences for low-mass galaxies and the impact of our extrapolations from the IR LFs.

We begin by noticing that previous authors reported a strong dependence of dust-obscured star formation with stellar mass as follows. The SFRs of galaxies with $M_* \gtrsim 10^9\ M_\odot$ are mainly traced by the IR light, while the FUV light is more important for lower-mass galaxies, and this trend is consistent with no redshift dependence (e.g., Pannella et al. 2009; Whitaker et al. 2017). If

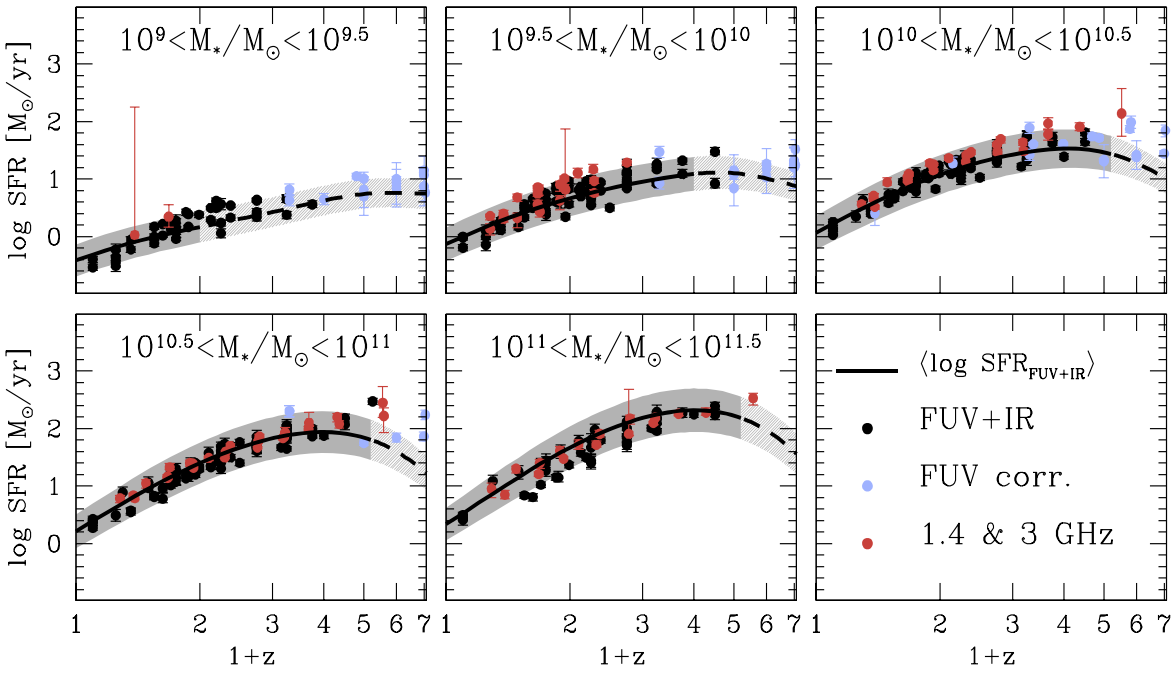

Figure 4. The SFRs as a function of redshift for five stellar mass bins. The solid lines show our results when the best-fitting models of both the FUV and IR LFs are available. The dashed lines show the mass regimes at the redshifts where the IR LFs have been extrapolated but the FUV LFs are available. The filled circles with error bars show the compilation reported from Table 3 for SFGs from galaxy surveys. Black circles show the results based on FUV+IR, while light blue and red circles show the results based on FUV dust-corrected and radio data. Note that this figure shows that our estimates of total SFRs inferred from fitting the FUV and IR LFs are in good agreement with direct measurements of the total SFR.

Table 3
SFRs

Author	SFR Indicator	Δ_{SFR} (dex)	Δ_{M_*}(dex)	σ_{SFR} (dex)	Redshift
Popesso et al. (2019b, 2019a)	UV+IR	0	0	0.25–0.4	$0 < z < 2.5$
Lee et al. (2015)	UV+IR	−0.15	0	0.36	$0.2 < z < 1.3$
Ilbert et al. (2015)	UV+IR	0	0	0.22–0.48	$0.2 < z < 1.4$
Whitaker et al. (2012)	UV+IR	−0.15	−0.03	0.34	$0.5 < z < 2.5$
Whitaker et al. (2014)	UV+IR	−0.13	0	0.34[a,b]	$0.5 < z < 2.5$
Tomczak et al. (2016)	UV+IR	−0.13	0	0.34[a,b]	$0.5 < z < 4$
Schreiber et al. (2015)	UV+IR	−0.31	−0.2	0.31	$z < 4$
Reddy et al. (2012)	UV+IR and SED	−0.2	−0.2	0.37	$1.4 < z < 3.7$
Tasca et al. (2015)	UV	0	0	∼0.54[c]	$0.4 \lesssim z \lesssim 4.8$
Bouwens et al. (2012)	UV	−0.3	−0.2	0.3[a,d]	$z \sim 4$
González et al. (2011)	UV	−0.2	−0.2	0[a]	$4 \lesssim z \lesssim 6$
Salmon et al. (2015)	UV	−0.2	−0.2	0.25–0.42	$4 \lesssim z \lesssim 6$
Duncan et al. (2014)	UV	0	0	0.17–0.36	$4 \lesssim z \lesssim 6$
Khusanova et al. (2020)	UV	0	0	0[a]	$5.5 < z < 6.6$
Karim et al. (2011)	1.4 GHz	+0.18[e]	−0.02	0[a]	$0.2 < z < 0.4$
Karim et al. (2011)	1.4 GHz	+0.15[e]	−0.02	0[a]	$0.4 < z < 0.6$
Karim et al. (2011)	1.4 GHz	+0.11[e]	−0.02	0[a]	$0.6 < z < 0.8$
Karim et al. (2011)	1.4 GHz	+0.07[e]	−0.02	0[a]	$0.8 < z < 1$
Karim et al. (2011)	1.4 GHz	+0.03[e]	−0.02	0[a]	$1 < z < 1.2$
Karim et al. (2011)	1.4 GHz	−0.01[e]	−0.02	0[a]	$1.2 < z < 1.6$
Karim et al. (2011)	1.4 GHz	−0.07[e]	−0.02	0[a]	$1.6 < z < 2.0$
Karim et al. (2011)	1.4 GHz	−0.12[e]	−0.02	0[a]	$2.0 < z < 2.5$
Leslie et al. (2020)	3 GHz	−0.1	0	0[a,d]	$0.3 < z < 6$

Notes. Here Δ_{SFR} and Δ_{M_*} are the logarithmic correction offsets. Corrections to the same IMF and when authors report ⟨SFR⟩ instead of ⟨logSFR⟩ were applied.
[a] No measure of the scatter is available.
[b] We assumed $\sigma_{SFR} = 0.34$ as in Whitaker et al. (2012).
[c] The authors reported that error bars were computed as $\sigma/\sqrt{N}$, where σ is the standard deviation around the sSFR distribution and N is the number of galaxies. Based on their values reported for the error bars, we find that, on average, $\sigma \sim 0.54$ dex.
[d] We assumed $\sigma_{SFR} = 0.3$.
[e] Corrections taken from Speagle et al. (2014).

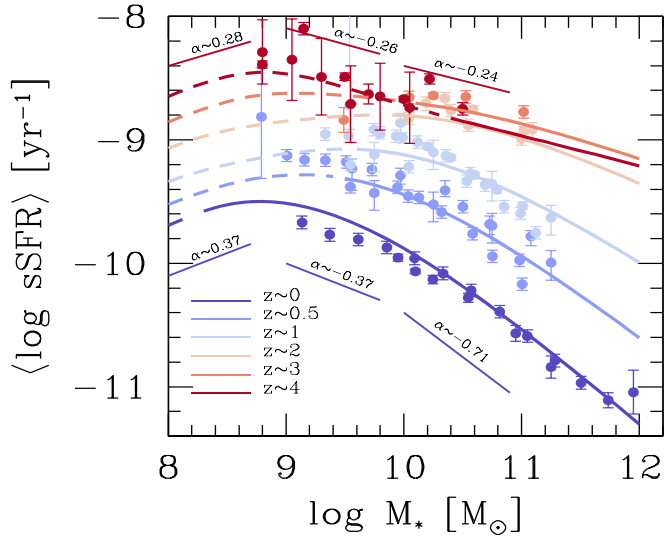

Figure 5. The sSFR–M_* relation for MS SFGs from $z \sim 0$ to 4. The solid lines show our results when the best-fitting models of both the FUV and IR LFs are available. The dashed lines show the mass regimes when the IR LFs have been extrapolated but the FUV LFs are available. The filled circles with error bars show the compilation from Table 3 for MS SFGs. Our results are consistent with the inferences from galaxy surveys. The slope, $\alpha = d\langle \mathrm{logsSFR}\rangle / d\log M_*$, at $z \sim 0$ for low masses, $M_* = 10^8$–$10^{8.8}$ $M_\odot$, is $\alpha \sim 0.37$, while for intermediate, $M_* = 10^9$–10^{10} $M_\odot$, and high, $M_* = 10^{10}$–10^{12} $M_\odot$, masses, we find that $\alpha \sim -0.37$ and $\sim$−0.71, respectively. At $z \sim 4$, the slopes for intermediate and high masses are, respectively, $\alpha \sim -0.26$ and −0.24, while at low masses, it is $\alpha \sim 0.28$.

we extrapolate the above results to our derivations, the implication is straightforward: for low-mass galaxies $M_* \lesssim 10^9$ $M_\odot$, the FUV LF is more important for the total SFR than the IR LF. In other words, little or no dust correction is required for the FUV-based SFRs of low-mass galaxies. In consequence, our resulting trends with mass and redshift for low-mass galaxies that are dominated by the FUV will be in the right direction. The above is also supported by Figures 8 and 9 below. In light of the above, we next describe our results for low-mass galaxies.

Figure 5 shows evidence that the sSFR–M_* relation for MS galaxies bends, and even the slope sign changes, at the low-mass end at all redshifts. Why does the sSFR–M_* relation change sign at the low-mass end? To answer this question, we use the fact that the SFRs from low-mass galaxies, $M_* \lesssim 10^9$ $M_\odot$, are dominated by the FUV component. The top and bottom panels of Figure 6 show the corresponding $M_{\rm FUV}$–M_* and $\mathrm{sSFR_{FUV}}$–M_* relationships. An important trend is apparent. The $\mathrm{sSFR_{FUV}}$–M_* relation bends below $M_* \sim 10^9$ $M_\odot$, similar to the sSFR–M_* relation. Not surprising, this bend is inherited by the turnover of the $M_{\rm FUV}$–M_* relation. The next important feature to notice is that the turnover mass of the $M_{\rm FUV}$–M_* relation is nearly constant with redshift, $\sim 5 \times 10^8$ $M_\odot$, but $M_{\rm FUV}$ changes from $M_{\rm FUV} \sim -16$ at $z \sim 0$ to $M_{\rm FUV} \sim -20$ at $z \sim 4$. By looking to Figure 2, it is then evident that the above magnitudes correspond to the knee of the FUV LF. It is now clear that the bending in the sSFR–M_* relation is due the knee of the FUV LF. In general, it is important to note that the forms of the $M_{\rm FUV}$–M_* and $\mathrm{sSFR_{FUV}}$–M_* relations are governed by the Schechter-like shapes of the FUV LF. Individual determinations for low-mass galaxies at high redshifts will be key to confirming the above and studying the self-consistency of the joint evolution of the faint end of the GSMF and the FUV+IR LFs. Fortunately, more accurate observational constraints are available at low masses for nearby galaxies, so we now focus our discussion on low-mass and dwarf galaxies at $z \sim 0$.

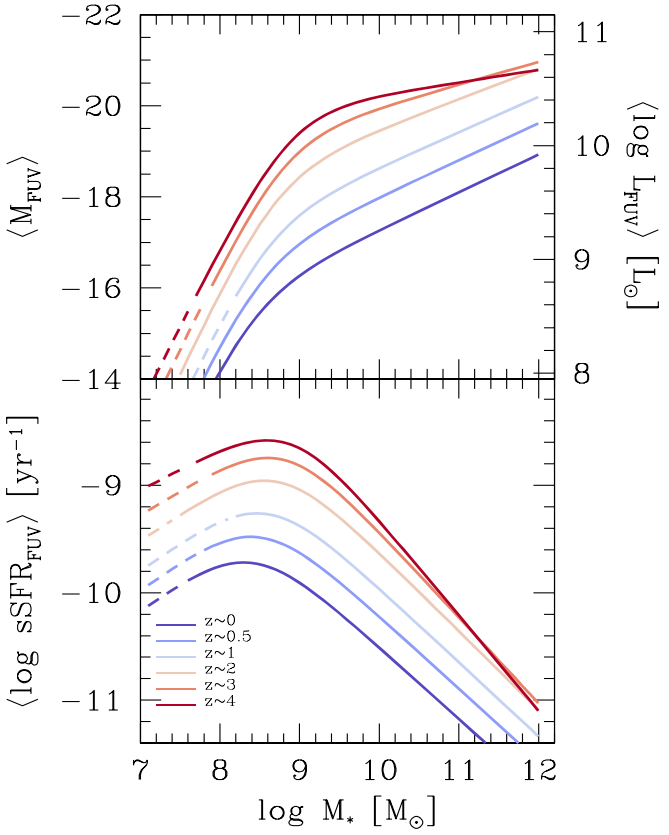

Figure 6. Top panel: $M_{\rm FUV}$–M_* relation for MS SFGs from $z \sim 0$ to 4. The solid lines show our results constrained by our best-fitting models of the FUV LF. The dashed lines show the mass regimes when the FUV LFs have been extrapolated. Bottom panel: $\mathrm{sSFR_{FUV}}$–M_* relation for MS SFGs from $z \sim 0$ to 4. Notice that the bend in the $\mathrm{sSFR_{FUV}}$–M_* relationship corresponds to the knee of the FUV LF (Figure 2).

Figure 7 again presents the sSFR–M_* relationship but this time at $z \sim 0$ and extending down to dwarf galaxies, $M_* \sim 7 \times 10^7$ $M_\odot$. As noted above, the slope of this relation flattens at low masses and changes sign around $M_* \sim 5 \times 10^8$ $M_\odot$. Additionally, we separately present the contribution to the SFRs from the FUV (blue solid line) and IR (red solid line). Notice that the mass around which the slope of the sSFR–M_* relationship changes sign is close to the mass above which the regime of dust-obscured star formation starts to dominate, $M_* \sim 6 \times 10^8$ $M_\odot$.

Similar to Figure 5, we compare our results with our compilation at $z \sim 0$ (gray stars with error bars). At low masses, we add our estimates of the (total) sSFRs to the KINGFISH sample from Skibba et al. (2011) obtained with the Galaxy Evolution Explorer (GALEX) and Herschel Space Observatory data (filled black circles). We also compute the average sSFR from a sample of low-mass galaxies at the mass range $10^{8.5} \lesssim M_*/M_\odot \lesssim 10^9$ with an axis ratio of $b/a \geqslant 0.5$ from the MaNGA/SDSS-IV survey (Cano-Diaz 2020, in preparation).[9] Finally, from a sample of dwarf galaxies from McGaugh et al. (2017), we compute the average sSFR at the mass range $10^{7.5} \lesssim M_*/M_\odot \lesssim 10^8$ (open square). Notice that, both for the MaNGA and the McGaugh et al. (2017) samples, the SFRs were derived from H_α luminosities. We transform

[9] The methodology to derive the SFRs and select the SF galaxies is explained in detail in Cano-Díaz et al. (2019). In this work, we use the data products provided by the Pipe3D Value Added Catalogue (Sánchez et al. 2018), which uses the integral field spectroscopy analysis pipeline, Pipe3D (Sánchez et al. 2016), for the last MaNGA public data release, version v2-4-3.

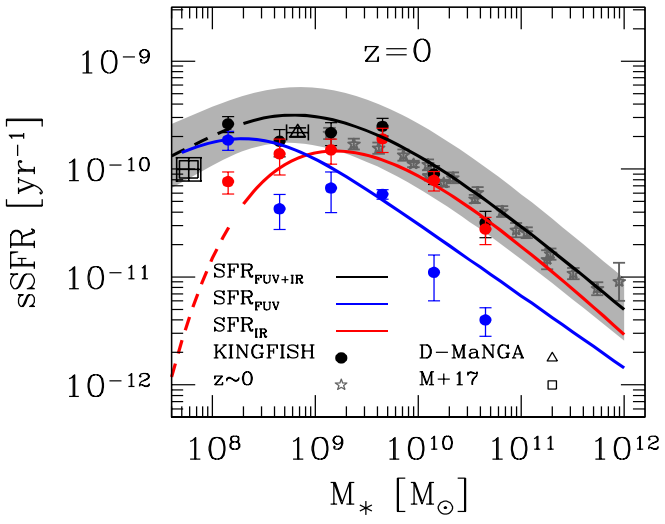

Figure 7. The sSFR–M_* relation for MS SFGs at $z \sim 0$ over a broad mass range: $M_* \sim 7 \times 10^7$–10^{12} $M_\odot$ (black solid line). The contributions from the FUV and IR are shown separately with blue and red solid lines, respectively. The gray stars with error bars correspond to the compilation from Table 3. The filled black circles corresponds to the total SFRs based on the KINGFISH sample from Skibba et al. (2011), while the blue and red filled circles correspond to the contributions from the FUV and IR, respectively. The open triangle shows the average sSFR from a sample of low-mass galaxies at the mass range $10^{8.5} \lesssim M_*/M_\odot \lesssim 10^9$ from the MaNGA/SDSS-IV survey (Cano-Diaz 2020, in preparation). The open square shows the results from a sample of dwarf galaxies from McGaugh et al. (2017) at $10^{7.5} \lesssim M_*/M_\odot \lesssim 10^8$. Our results are consistent with this set of independent observations for local galaxies.

their H_α determinations into dust-corrected SFR_{FUV} by using Equation (16) from Shin et al. (2020). In general, our results for the total SFRs are in good agreement with the above set of observations down to $M_* \sim 7 \times 10^7$ $M_\odot$.

In the case of the KINGFISH sample, the authors reported IR luminosities (see their Table 1), which we transform into SFRs (red circles). We also subtract IR SFRs from the total in order to compute UV SFRs (blue circles) according to their Equation (7). It is encouraging that our results reproduce pretty well the observational trends from the KINGFISH sample. Remarkably, both our results and the KINGFISH sample appear to have a similar characteristic mass, $M_{*,obsc} \sim 6 \times 10^8$ $M_\odot$, above which the SFRs are dust-obscured. We thus confirm that the FUV light becomes more important as a diagnostic of the SFRs of dwarf galaxies.

3.2. The Redshift Evolution of the FUV and IR Contribution to the Total SFR

In Figure 8, we explore the contribution of the FUV and IR to the total sSFR–M_* relationship at $0.5 \leqslant z \leqslant 2.5$. Similar to Figure 5, the solid lines show the mass regime where the best-fitting models of both the FUV and IR LFs are constrained by the data, while the dashed lines show the stellar mass regime where the LFs were extrapolated.

We compare our results to the total SFRs reported from Whitaker et al. (2014) computed as the combination of the UV[10] and IR values based on Spitzer/MIPS 24 μm photometry. Note that we subtract ~0.13 dex from their SFRs in order to convert from $\log\langle \mathrm{sSFR} \rangle$ to $\langle \log \mathrm{sSFR} \rangle$; see Equation (4) and Table 3. In the same figure, we separately present the contribution from FUV and IR by using the average luminosities, $\langle L \rangle (M_*)$, reported in their Table 2. Note that we plotted two different symbols for the SFR_{FUV} from Whitaker et al. (2014). The open

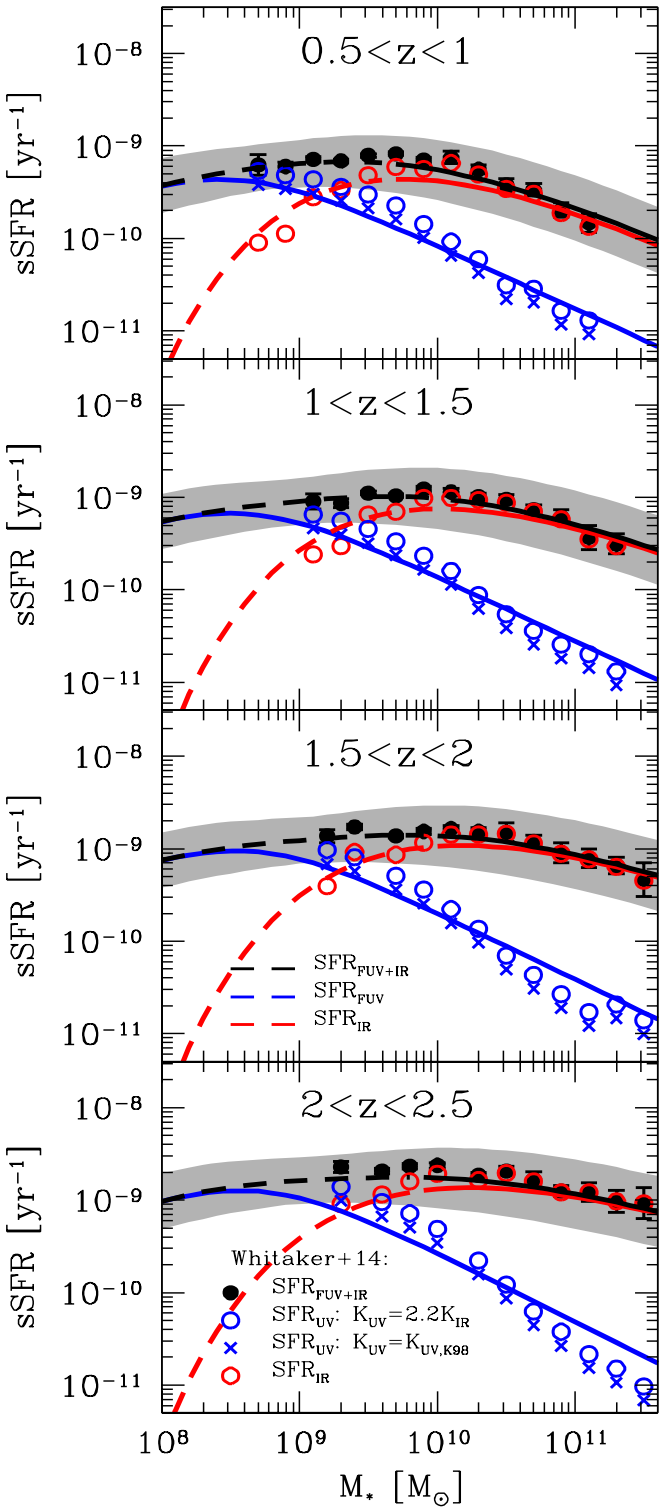

Figure 8. Predicted total average sSFR–M_* relation and the contribution from FUV and IR light from $z = 0.5$ to 2.5. We compare to the inferences from Whitaker et al. (2014). Similar to Figure 5, the solid lines show our resulting sSFRs where both the best-fitting models from the FUV and IR LFs are valid, while the dashed lines show where the FUV LF is valid but the IR LF has been extrapolated. Our results are consistent with the total SFRs from Whitaker et al. (2014), as well as the FUV and IR contributions, even in the regimes where we have extrapolated our results.

[10] Whitaker et al. (2014) estimated UV luminosities as the integrated light within the range between 1260 and 3000 Å by using the 2800 Å rest-frame luminosity: $L_{UV}(1260-3000\ \text{Å}) = 1.5\nu L_{\nu,2800}$.

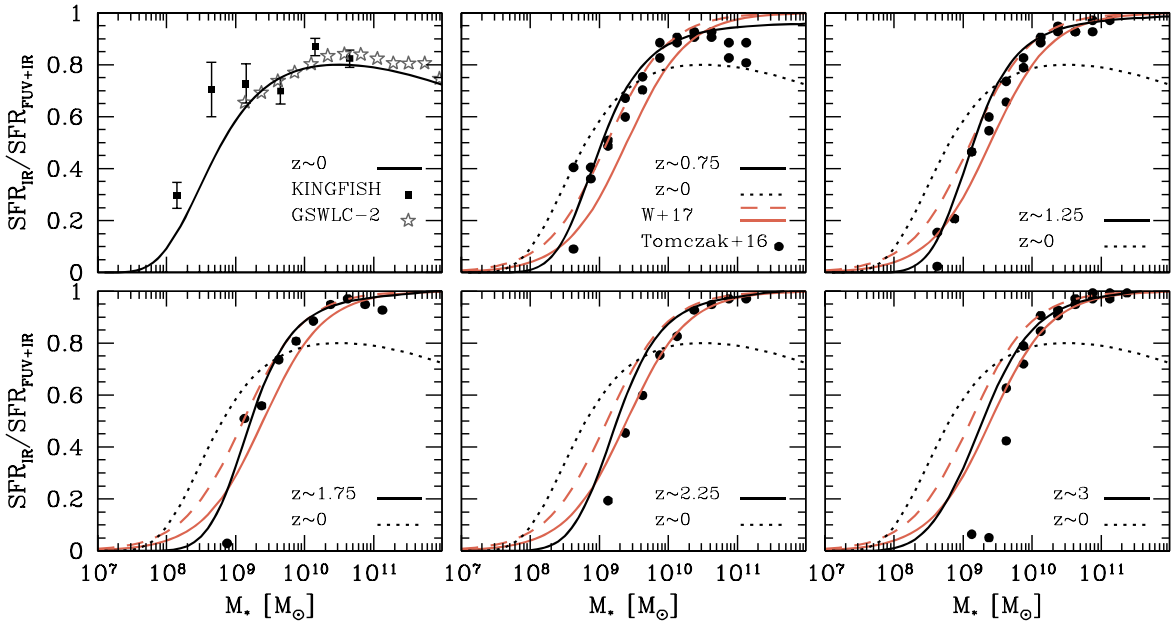

Figure 9. Redshift evolution for the fraction of obscured star formation as a function of M_*. The solid lines show our results at the redshifts indicated by the labels, while the dotted lines reproduce our results for local galaxies. It is clear that the fraction of dust-obscured star formation evolves with redshift. We present comparisons with the local determinations based on the KINGFISH sample (Skibba et al. 2011; filled black squares) and the dust attenuation values $A_{\rm FUV}$ reported in the GSWLC-2 (Salim et al. 2018; open gray stars). At high redshift, we reproduce the results from Tomczak et al. (2016; filled circles) based on their reported luminosities $\langle L_{\rm FUV}\rangle$ and $\langle L_{\rm IR}\rangle$. The red solid line is the best fit to the observations from Whitaker et al. (2017) using the FUV estimator from Whitaker et al. (2014), while the red dashed line shows their results based on the Murphy et al. (2011) FUV estimator.

circles show the conversion factor utilized by Whitaker et al. (2014) of $\mathcal{K}_{\rm FUV} = 2.2 \times \mathcal{K}_{\rm IR} = 2.4 \times 10^{-10} M_\odot$ yr$^{-1} L_\odot^{-1}$, while the crosses use the conversion factor utilized in this paper; see Section 2. The conversion factor used by Whitaker et al. (2014) is a factor of ∼1.4 larger than ours. Thus, the crosses are more adequate for comparing with our results.

In general, when comparing to Whitaker et al. (2014), we observe that our results capture the same trends for the contributions from the FUV and IR at all masses and redshifts, even for the regimes where we extrapolated our results from the IR LFs (red dashed lines). Note that the FUV component dominates the low-mass regime both in our and in Whitaker et al.'s (2014) results. This is encouraging and hints again that the trends reported in Figures 5 and 7 for the total SFRs at the low-mass regime are in the right direction.

Regarding the characteristic mass, $M_{*,\rm obsc}$, where $\rm SFR_{FUV}$ and $\rm SFR_{IR}$ are equal, or, equivalently, the transition mass to the dust-obscured star formation regime, we observe an increase in mass by a factor of ∼3.3 from $z \sim 0$ to 2.5; the values are, respectively, $M_{*,\rm obsc} \sim 6 \times 10^8$ and $\sim 2 \times 10^9$ $M_\odot$. From $z \sim 0.5$ to 2.5, the characteristic mass has increased by a factor of ∼2.2. A similar trend is observed based on the results from Whitaker et al. (2014) and reported explicitly in Whitaker et al. (2017).

3.3. Mass and Redshift Dependence of the Obscured Star Formation Regime

According to Figures 7 and 8, our results are consistent with observational samples that separate the contributions from the FUV and IR from $z \sim 0$ to 2.5, even when we extrapolated our results for the IR LFs. In the following, we will use our results based on the extrapolations of the IR LFs as direct predictions from our approach.

The top left panel of Figure 9 presents our resulting fraction of dust-obscured star formation as a function of stellar mass at $z \sim 0$ (black solid line). Our results show a strong dependence with stellar mass in the direction that the SFRs of high-mass galaxies are more obscured by dust than low-mass galaxies. At $M_* \sim 10^{10}$ $M_\odot$, the dust-obscured fraction approaches a maximum value of ∼0.8, and for larger masses, it keeps roughly constant. The filled circles show the results from the KINGFISH sample. The gray stars show the results of using the dust attenuation values $A_{\rm FUV}$ reported in the GSWLC-2 catalog. Both the KINGFISH sample and the GSWLC-2 catalog are in good agreement with our results. Next, we discuss the comparison with high-redshift data.

The remaining panels of Figure 9 present the fraction of dust-obscured star formation as a function of stellar mass from $z \sim 0.75$ to 3. In each panel, the $z \sim 0$ curve is repeated with the dotted line. As seen from the sequence of panels, the fraction of dust-obscured SFRs evolves mostly from $z \sim 0$ to 1.2, but above $z \sim 1.2$, our results are consistent with little evolution up to $z \sim 3$. Thus, our results indicate that the fraction of dust-obscured SFRs evolves with redshift. We also reproduce the best-fitting model for the fraction of dust-obscured SFRs from Whitaker et al. (2017) at $0.5 \leqslant z \leqslant 2.5$ using their "standard calibration" (black solid line) and best-fitting model based on the Murphy et al. (2011) calibration parameters (dashed lines). Notice the agreement between our results and those from Whitaker et al. (2017) when considering both of their calibrators. We also compute the fraction of dust-obscured SFRs using the luminosities $\langle L_{\rm FUV}\rangle$ and $\langle L_{\rm IR}\rangle$ reported in Table 1 from Tomczak et al. (2016; filled circles).

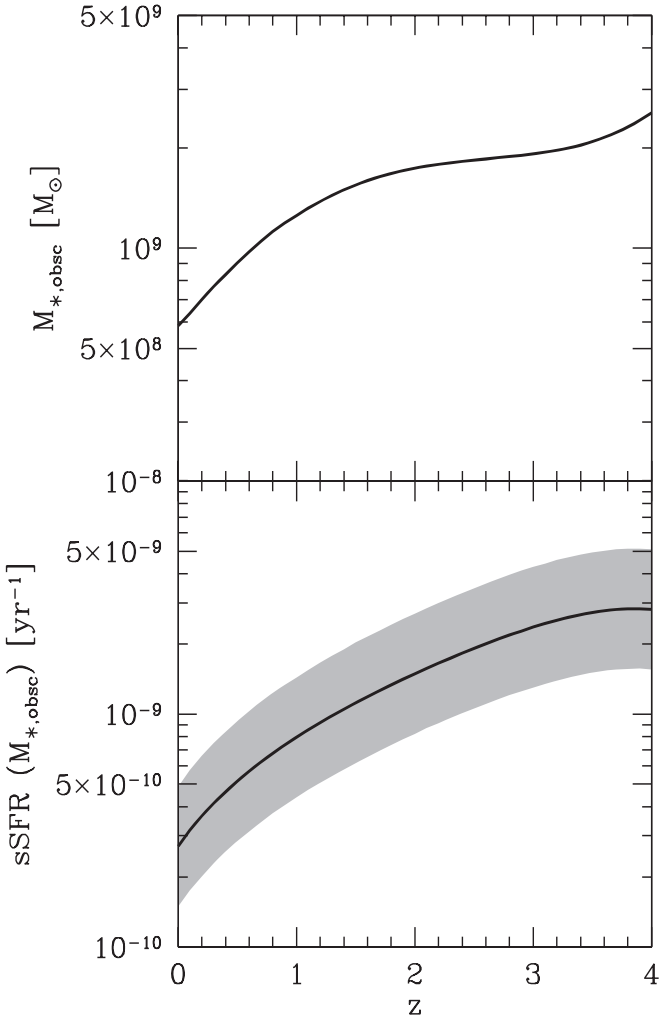

Figure 10. Top panel: redshift evolution of the characteristic mass $M_{*,\mathrm{obsc}}$ that marks the transition between the unobscured and obscured star formation regimes. Notice that since $z \sim 1.5$, the characteristic mass $M_{*,\mathrm{obsc}}$ decreased by a factor of $\sim$4, while above $z \sim 1.5$, it increased only slowly. Bottom panel: corresponding total sSFR of the characteristic mass $M_{*,\mathrm{obsc}}$. The sSFR has decreased by an order of magnitude since $z \sim 4$.

We find that our results are consistent with these authors, including the increase in $M_{*,\mathrm{obsc}}$ with redshift.

An important feature is worth mentioning here. According to our results, at low redshifts, $z \lesssim 0.75$, high-mass galaxies have become more "transparent" to UV light compared to their high-redshift counterparts. For low- and intermediate-mass galaxies, we observe the opposite: they have become more obscured by dust. Similar trends are derived when using the Tomczak et al. (2016) dust-obscured fractions.

The top panel of Figure 10 presents the evolution of the characteristic mass, $M_{*,\mathrm{obsc}}$, at which the fraction of dust-obscured star formation is 0.5 based on our model. Here the rapid evolution of $M_{*,\mathrm{obsc}}$ for $z \lesssim 1.2$ is evident, but then it rises only slowly at high redshifts up to a mass of $M_{*,\mathrm{obsc}} \sim 2 \times 10^9\ M_\odot$, as noted previously. The bottom panel shows the corresponding sSFR of $M_{*,\mathrm{obsc}}$. The sSFR($M_{*,\mathrm{obsc}}$) has a strong correlation with z and appears to reach a maximum of sSFR $\sim 3 \times 10^{-9}$ yr^{-1} just before $z \sim 4$. The sSFR($M_{*,\mathrm{obsc}}$)–redshift relation has decreased by an order of magnitude since $z \sim 4$.

4. Summary and Discussion

In this paper, we present an analytical method for deriving the evolution of the mean sSFR–M_* relation of MS galaxies by combining the FUV and IR rest-frame LFs with the GSMF of SFGs from $z \sim 0$ to 4. The total SFR is estimated as the sum of the unobscured and obscured regimes traced by the FUV (1500 Å) and IR (8–1000 μm) luminosities, respectively. Our approach is an alternative to the commonly employed procedure in the literature, consisting of using large galaxy samples for which the masses and SFRs are inferred individually for every galaxy. As discussed in Section 2, the determination and understanding of the SFR–M_* relation and its evolution for MS galaxies can be affected due to (i) intrinsic selection effects in large galaxy samples and (ii) the comparison of SFRs based on different tracers and estimations not being trivial. In our approach, this is not the case, since the evolution of the MS is derived from the FUV and IR LFs and the GSMF, distributions that are complete in volume, luminosities, and mass over a large redshift range. Our main results are as follows.

1. The homogeneously obtained SFRs as a function of M_* for MS galaxies at redshifts $0 \lesssim z \lesssim 4$ confirm and unify, within the scatter, the values obtained previously from different galaxy surveys that used a diversity of SFR tracers and methods; see Figure 4.
2. Our methodology allows for consistent inferences of the mean sSFR–M_* relationships for MS galaxies down to low masses. Moreover, it allows for reasonable extrapolations down to the regime of dwarf galaxies, where the unobscured FUV component dominates the total SFR; see Figures 5 and 7.
3. The mean sSFR–M_* relation for MS galaxies bends strongly at low masses, $\lesssim 10^9\ M_\odot$, and the slope sign changes from positive at low masses to negative at intermediate and high masses masses at all redshifts. In particular, at $z \sim 0$, the slope changes between $\sim$0.37 and ~ -0.37 at low to intermediate masses. The bending in the MS at lower masses is connected to the knee of the FUV LF; see Figure 6.
4. At $z \sim 0$, the change of sign in the MS occurs around $M_* \sim 5 \times 10^8\ M_\odot$, which is close to the dust-obscured star formation regime at this redshift, $M_* \sim 6 \times 10^8\ M_\odot$.
5. At $z \sim 0$, the resulting contributions from unobscured (FUV) and obscured (IR) SFRs are in good agreement with the results from the KINGFISH sample (based on GALEX and Herschel Space Observatory data) and the dust attenuation values A_{FUV} reported in the GSWLC-2 (based on GALEX, SDSS, and WISE). At $0.5 \lesssim z \lesssim 2.5$, we show that our results capture the observed trends to the contributions from the FUV and IR to the total SFRs from Whitaker et al. (2014).
6. At all redshifts, the contribution from the FUV dominates the total sSFR–M_* relation at low masses; see Figures 8 and 9. The characteristic mass for the obscured SFR regime has decreased by a factor of $\sim$3 since $z \sim 4$: $M_{*,\mathrm{obsc}} \sim 2 \times 10^9\ M_\odot$ at $z \sim 4$ and $M_{*,\mathrm{obsc}} \sim 6 \times 10^8\ M_\odot$ at $z \sim 0$; see Figure 10.
7. The fraction of obscured SFRs, $\mathrm{SFR_{IR}}/\mathrm{SFR_{FUV+IR}}$, depends strongly on mass and changes very little with redshift for $z > 1.2$, in agreement with Tomczak et al. (2016) and Whitaker et al. (2017); see Figure 9. Below

$z \sim 0.75$, galaxies more massive than $\sim 10^{10}\ M_{\odot}$ become more "transparent" than high-redshift galaxies with the same stellar mass, while for low-mass galaxies, the opposite is true, as they become more obscured by dust at the same stellar mass; see Figure 9.

According to our results, the sSFR–M_* relation bends and changes its slope sign from positive at low masses to negative at high masses. At $z \sim 0$, this change occurs at $M_* \sim 5 \times 10^8\ M_{\odot}$. This has interesting implications for dwarf galaxies. If we interpret the inverse of the total sSFR as the characteristic time that it will take a galaxy to double its mass at a constant SFR, then the above implies that dwarf MS galaxies, $M_* \lesssim 5 \times 10^8\ M_{\odot}$, form stars at a slower pace than intermediate-mass MS galaxies, $10^9 \lesssim M_*/M_{\odot} \lesssim 10^{10}$. For our low-mass limit of $M_* \sim 7 \times 10^7\ M_{\odot}$, we find that sSFR $\sim 10^{-10}$ yr^{-1}; see Figure 7. Assuming a constant SFH, this implies an assembling time of $\sim$10 Gyr. Observations of nearby dwarf galaxies show a significant mass fraction, $\gtrsim$30%, in stellar populations older than 10–11 Gyr (Weisz et al. 2014), consistent with our estimation. Note that if the sSFRs of low-mass galaxies would follow the same trend with M_* as the one for $M_* \gtrsim 10^9\ M_{\odot}$, then the assembling time would be $\lesssim$2 Gyr. That is, dwarf galaxies would be just in their process of formation, in clear disagreement with our results and the resolved SFHs from nearby dwarf galaxies.

There are other observational works of local star-forming dwarf galaxies that also show that their mean sSFR–M_* relation bends with respect to the MS at higher masses (e.g., McGaugh et al. 2017; Davies et al. 2019). However, in these works, the slope of the low-mass MS is not as steep as in our case, though this is difficult to evaluate, since the scatter of the MS increases at lower masses (see, e.g., Davies et al. 2019). Motivated by the above, we have repeated our calculations at $z \sim 0$ by increasing the scatter only for the FUV contribution from 0.3 to 0.5 dex (recall that for low-mass galaxies, the FUV is more important). We find that the slope at low masses of the resulting mean sSFR–M_* relation becomes slightly shallower as compared to the results based on the dispersion of 0.3 dex. More accurate observational studies of low-mass and, in particular, dwarf galaxies will be key to confirming the bend of the mean sSFR–M_* relation.

Studying the joint evolution of the FUV and IR rest-frame LFs and the GSMF appears as a promising and powerful approach to understanding the contribution of unobscured (FUV) and obscured (IR) components to the total SFRs as a function of M_* and z and ultimately to constraining models of the formation and destruction of dust in galaxies.

The increase of heavy-element abundances in any galaxy, and hence of its dust content, is a direct result of stellar activity. As stated by several authors (see discussions by Dwek & Cherchneff 2011 and Slavin et al. 2020 and references therein), the expanding ejecta from supernovae is perhaps the main source of dust at high redshifts. Our results suggest that there seems to be a feedback mechanism between the formation of dust and the star-forming activity. For high-mass galaxies at early stages of evolution, the vigorous star-forming activity supplies the ambient interstellar medium with a generous amount of recently formed dust. This may provide the required opacity to shield the neighboring gas from the stellar UV radiation (e.g., Franco & Cox 1986), stimulating the formation of new generations of molecular clouds. This, in turn, induces the conditions for further star formation, but the strong energy injection, both radiative and mechanical, is highly disruptive and tends to destroy the clouds, restricting the outcome of the star formation process. Regardless of the evolution of the resulting SFR, the emerging luminosity proceeds in a dust-obscured fashion. For the case of low-mass galaxies, in contrast, with a smaller SFR and weaker gravitational field than their massive counterparts, the evolution proceeds at a slower rate with a milder supernova rate and a slowly growing metal content. The stellar energy injection in this case can be more disruptive and even expel the interstellar gas and recently formed dust out of the galaxy (e.g., Caproni et al. 2015), leading to a more transparent evolutionary mode. It is not clear, however, why the dust-obscured fraction evolves mostly below $z \sim 1$, and there is little evolution between $z \sim 1.5$ and 4. Perhaps our results indicate that dust cycling is not the full story, but the spatial distribution of dust and its dependence on disk secular evolution might play a relevant role (e.g., Dalcanton et al. 2004). These scenarios will be explored in more detail in a future publication.

Future research should be focused on extending the consistency between the GSMF and the evolution of FUV and IR LFs to lower-mass and higher-redshift regimes. Here we found that this is the case at $z \sim 4$ and for $10^9 \lesssim M_*/M_{\odot} \lesssim 10^{11.5}$ by being in agreement with the observed trends of the sSFR–M_* relationship and the dust-obscured fraction results obtained directly from galaxy surveys. Extending the semiempirical modeling like that presented in Rodríguez-Puebla et al. (2017), Moster et al. (2018), Tacchella et al. (2018), and Behroozi et al. (2019) to include FUV and IR LFs looks very promising and timely to understand how dark matter halos build their stellar mass and the evolution of dust in their host galaxies (Rodríguez-Puebla et al. 2020, in preparation). In addition, more theoretical work will be needed in order to understand the role of the dust and the trends with the fraction of obscured SFRs derived here.

We thank the anonymous referee for a constructive report that helped to improve this paper. A.R.P. and V.A.R. acknowledge support from UNAM PAPIIT grant IA104118 and CONACyT "Ciencia Basica" grant 285721. This project makes use of the MaNGA-Pipe3D data products. We thank the IA-UNAM MaNGA team for creating this catalog and the CONACYT-180125 project for supporting them.

Appendix
The GSMF

We define the GSMF for all (including SF and quenched) galaxies as the sum of two modified Schechter components,

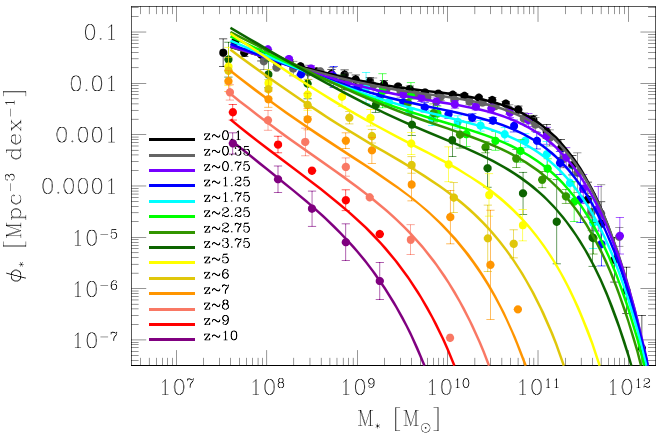

Figure 11. Best-fitting model for the redshift evolution of the GSMF from Rodríguez-Puebla et al. (2017) .

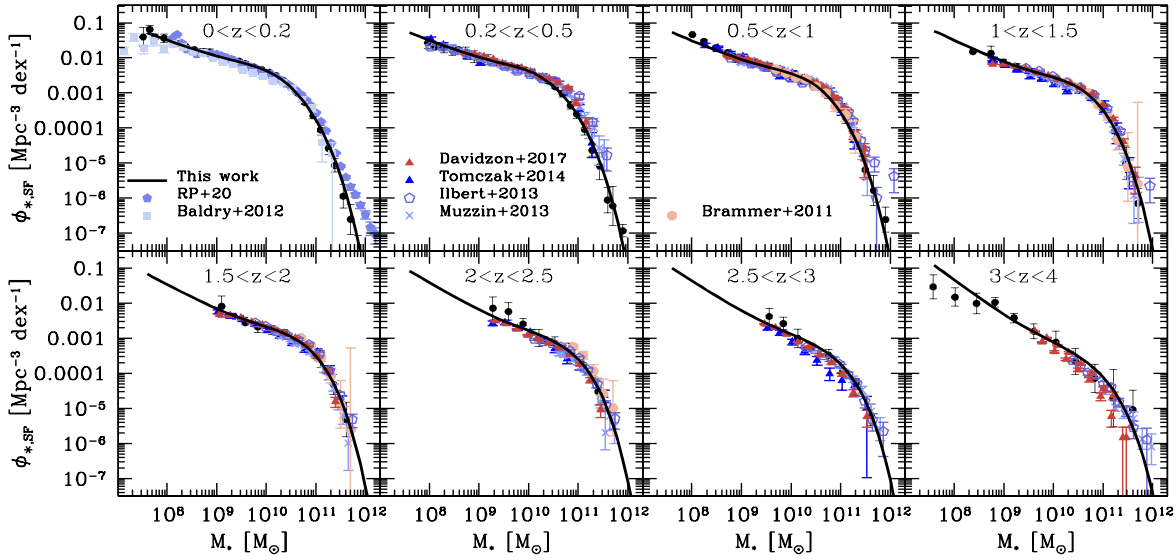

Figure 12. The GSMFs of SFGs at various redshifts. We compare our model for the GSMFs of SFGs (solid line) with different authors based on local (Baldry et al. 2012; Rodríguez-Puebla et al. 2020) and high-redshift (Brammer et al. 2011; Ilbert et al. 2013; Muzzin et al. 2013; Tomczak et al. 2014; Davidzon et al. 2017) measurements. In general, we observe a good agreement between the different authors and our model; however, the comparison should be taken with care, as the definition of SFG could vary between authors.

$\phi_* = \phi_{*,1} + \phi_{*,2}$:

$$\phi_{*,i}(M_*) = \phi_i^* \left(\frac{M_*}{M_i}\right)^{1+\alpha_i} \exp\left[-\left(\frac{M_*}{M_i}\right)^{\beta_i}\right]. \quad \text{(A1)}$$

We assume that $\beta_1 = 1$, $\phi_2^* = 6 \times \phi_1^*$, $M = M_1 = M_2$, and $\alpha_2 = 1 + \alpha_1$. The above guarantees that the first component is a Schechter function, while the second component is a modified Schechter component dominating the massive end, $M_* \gtrsim M_i$, of the GSMF. Similar to the LFs, we integrate our mass function over the redshift range in which the GSMF is being observed: $\phi_{\rm obs}(z_i, z_f) = \int \phi_*(z) dV(z) / (V_i - V_f)$. The best-fitting models for the compilation from Rodríguez-Puebla et al. (2017) are

$$\alpha(z) = (-1.758 \pm 0.026) + \log(\mathcal{S}(z;\, 0,\, 2.815 \pm 0.297,\, 2.085 \pm 0.187,\, 0)), \quad \text{(A2)}$$

$$\log\left(\frac{\phi_1^*(z)}{\rm Mpc^{-3} dex^{-1}}\right) = (-3.161 \pm 0.070) + \log(\mathcal{S}(z;\, 0,\, 1.472 \pm 0.183,\, 2.538 \pm 0.252,\, 0)), \quad \text{(A3)}$$

$$\log\left(\frac{M(z)}{M_\odot}\right) = (-10.204 \pm 0.118) + \log(\mathcal{S}(z;\, 5.529 \pm 0.229,\, 6.961 \pm 0.423,\, -0.338 \pm 0.139)), \quad \text{(A4)}$$

and

$$\beta = 0.611 \pm 0.037. \quad \text{(A5)}$$

Here the function $\mathcal{S}$ is a double power law that depends on z and has three free parameters (p_1, p_2, p_3):

$$\mathcal{S}(z;\, p_1, p_2, p_3) = 2\left[\left(\frac{1+z}{p_1}\right)^{p_2} + \left(\frac{1+z}{p_1}\right)^{p_4}\right]^{-1}. \quad \text{(A6)}$$

Notice that p_1 is equivalent to a characteristic redshift at which the function $\mathcal{S}$ transits from the power law p_2 to p_3. In addition, at $p_1 = 1 + z$, $\mathcal{S} = 1$. Figure 11 compares our best-fitting model with observations. Finally, in order to compute the GSMF of SFGs, we use the fraction of SFGs from Rodríguez-Puebla et al. (2017), described in their Section 4.4. Figure 12 compares our resulting GSMF of SFGs to several measurements from the literature.

ORCID iDs

Aldo Rodríguez-Puebla https://orcid.org/0000-0002-0170-5358
Vladimir Avila-Reese https://orcid.org/0000-0002-3461-2342
Mariana Cano-Díaz https://orcid.org/0000-0001-9553-8230
Joel R. Primack https://orcid.org/0000-0001-5091-5098
I. Aretxaga https://orcid.org/0000-0002-6590-3994

References

Alavi, A., Siana, B., Richard, J., et al. 2014, ApJ, 780, 143
Alavi, A., Siana, B., Richard, J., et al. 2016, ApJ, 832, 56
Arnouts, S., Schiminovich, D., Ilbert, O., et al. 2005, ApJL, 619, L43
Atek, H., Richard, J., Kneib, J.-P., & Schaerer, D. 2018, MNRAS, 479, 5184
Baldry, I. K., Driver, S. P., Loveday, J., et al. 2012, MNRAS, 421, 621
Behroozi, P., Wechsler, R. H., Hearin, A. P., & Conroy, C. 2019, MNRAS, 488, 3143
Bernhard, E., Béthermin, M., Sargent, M., et al. 2014, MNRAS, 442, 509
Béthermin, M., Doré, O., & Lagache, G. 2012, A&A, 537, L5
Bhatawdekar, R., Conselice, C. J., Margalef-Bentabol, B., & Duncan, K. 2019, MNRAS, 486, 3805
Bouché, N., Dekel, A., Genzel, R., et al. 2010, ApJ, 718, 1001
Bouwens, R. J., Illingworth, G. D., Franx, M., & Ford, H. 2007, ApJ, 670, 928
Bouwens, R. J., Illingworth, G. D., Oesch, P. A., et al. 2011, ApJ, 737, 90
Bouwens, R. J., Illingworth, G. D., Oesch, P. A., et al. 2012, ApJ, 754, 83
Bouwens, R. J., Illingworth, G. D., Oesch, P. A., et al. 2015, ApJ, 803, 34
Brammer, G. B., Whitaker, K. E., van Dokkum, P. G., et al. 2011, ApJ, 739, 24
Brinchmann, J., Charlot, S., White, S. D. M., et al. 2004, MNRAS, 351, 1151
Burgarella, D., Buat, V., Gruppioni, C., et al. 2013, A&A, 554, A70
Cano-Díaz, M., Ávila-Reese, V., Sánchez, S. F., et al. 2019, MNRAS, 488, 3929
Cano-Díaz, M., Sánchez, S. F., Zibetti, S., et al. 2016, ApJL, 821, L26

Caproni, A., Lanfranchi, G. A., da Silva, A. L., & Falceta-Gonçalves, D. 2015, ApJ, 805, 109
Casey, C. M., Berta, S., Béthermin, M., et al. 2012, ApJ, 761, 140
Chabrier, G. 2003, PASP, 115, 763
Conselice, C. J., Wilkinson, A., Duncan, K., & Mortlock, A. 2016, ApJ, 830, 83
Cucciati, O., Tresse, L., Ilbert, O., et al. 2012, A&A, 539, A31
da Cunha, E., Charlot, S., & Elbaz, D. 2008, MNRAS, 388, 1595
Daddi, E., Dickinson, M., Morrison, G., et al. 2007, ApJ, 670, 156
Dalcanton, J. J., Yoachim, P., & Bernstein, R. A. 2004, ApJ, 608, 189
Davé, R., Finlator, K., & Oppenheimer, B. D. 2012, MNRAS, 421, 98
Davidzon, I., Ilbert, O., Laigle, C., et al. 2017, A&A, 605, A70
Davies, L. J. M., Lagos, C. d. P., Katsianis, A., et al. 2019, MNRAS, 483, 1881
Driver, S. P., Andrews, S. K., da Cunha, E., et al. 2018, MNRAS, 475, 2891
Driver, S. P., Robotham, A. S. G., Kelvin, L., et al. 2012, MNRAS, 427, 3244
Duncan, K., Conselice, C. J., Mortlock, A., et al. 2014, MNRAS, 444, 2960
Dwek, E., & Cherchneff, I. 2011, ApJ, 727, 63
Elbaz, D., Daddi, E., Le Borgne, D., et al. 2007, A&A, 468, 33
Fang, J. J., Faber, S. M., Koo, D. C., et al. 2018, ApJ, 858, 100
Finkelstein, S. L., Ryan, R. E., Jr., Papovich, C., et al. 2015, ApJ, 810, 71
Franco, J., & Cox, D. P. 1986, PASP, 98, 1076
Gavazzi, G., Consolandi, G., Dotti, M., et al. 2015, A&A, 580, A116
González, V., Labbé, I., Bouwens, R. J., et al. 2011, ApJL, 735, L34
Gruppioni, C., Pozzi, F., Rodighiero, G., et al. 2013, MNRAS, 432, 23
Hathi, N. P., Ryan, R. E. J., Cohen, S. H., et al. 2010, ApJ, 720, 1708
Ilbert, O., Arnouts, S., Le Floc'h, E., et al. 2015, A&A, 579, A2
Ilbert, O., McCracken, H. J., Le Fèvre, O., et al. 2013, A&A, 556, A55
Iyer, K., Gawiser, E., Davé, R., et al. 2018, ApJ, 866, 120
Karim, A., Schinnerer, E., Martínez-Sansigre, A., et al. 2011, ApJ, 730, 61
Kennicutt, Robert C. J. 1998, ARA&A, 36, 189
Khusanova, Y., Le Fèvre, O., Cassata, P., et al. 2020, A&A, 634, A97
Kilerci Eser, E., & Goto, T. 2018, MNRAS, 474, 5363
Kurczynski, P., Gawiser, E., Acquaviva, V., et al. 2016, ApJL, 820, L1
Le Floc'h, E., Papovich, C., Dole, H., et al. 2005, ApJ, 632, 169
Lee, B., Giavalisco, M., Whitaker, K., et al. 2018, ApJ, 853, 131
Lee, N., Sanders, D. B., Casey, C. M., et al. 2015, ApJ, 801, 80
Leslie, S. K., Schinnerer, E., Liu, D., et al. 2020, ApJ, 899, 58
Lim, C.-F., Wang, W.-H., Smail, I., et al. 2020, ApJ, 889, 80
Liu, D., Daddi, E., Dickinson, M., et al. 2018, ApJ, 853, 172
Livermore, R. C., Finkelstein, S. L., & Lotz, J. M. 2017, ApJ, 835, 113
Madau, P., & Dickinson, M. 2014, ARA&A, 52, 415
Magnelli, B., Elbaz, D., Chary, R. R., et al. 2011, A&A, 528, A35
Magnelli, B., Popesso, P., Berta, S., et al. 2013, A&A, 553, A132
McGaugh, S. S., Schombert, J. M., & Lelli, F. 2017, ApJ, 851, 22
Mehta, V., Scarlata, C., Rafelski, M., et al. 2017, ApJ, 838, 29
Moster, B. P., Naab, T., & White, S. D. M. 2018, MNRAS, 477, 1822
Murphy, E. J., Condon, J. J., Schinnerer, E., et al. 2011, ApJ, 737, 67
Muzzin, A., Marchesini, D., Stefanon, M., et al. 2013, ApJ, 777, 18
Noeske, K. G., Weiner, B. J., Faber, S. M., et al. 2007, ApJL, 660, L43
Novak, M., Smolčić, V., Delhaize, J., et al. 2017, A&A, 602, A5
Oesch, P. A., Bouwens, R. J., Carollo, C. M., et al. 2010, ApJL, 725, L150
Oesch, P. A., Bouwens, R. J., Illingworth, G. D., et al. 2012, ApJ, 759, 135
Ono, Y., Ouchi, M., Harikane, Y., et al. 2018, PASJ, 70, S10
Pannella, M., Carilli, C. L., Daddi, E., et al. 2009, ApJL, 698, L116
Parsa, S., Dunlop, J. S., McLure, R. J., & Mortlock, A. 2016, MNRAS, 456, 3194
Popesso, P., Concas, A., Morselli, L., et al. 2019a, MNRAS, 483, 3213
Popesso, P., Morselli, L., Concas, A., et al. 2019b, MNRAS, 490, 5285
Reddy, N. A., Pettini, M., Steidel, C. C., et al. 2012, ApJ, 754, 25
Reddy, N. A., & Steidel, C. C. 2009, ApJ, 692, 778
Robotham, A. S. G., & Driver, S. P. 2011, MNRAS, 413, 2570
Rodighiero, G., Daddi, E., Baronchelli, I., et al. 2011, ApJL, 739, L40
Rodighiero, G., Vaccari, M., Franceschini, A., et al. 2010, A&A, 515, A8
Rodríguez-Puebla, A., Avila-Reese, V., & Drory, N. 2013, ApJ, 767, 92
Rodríguez-Puebla, A., Calette, A. R., Avila-Reese, V., Rodriguez-Gomez, V., & Huertas-Company, M. 2020, PASA, 37, e024
Rodríguez-Puebla, A., Primack, J. R., Avila-Reese, V., & Faber, S. M. 2017, MNRAS, 470, 651
Salim, S., Boquien, M., & Lee, J. C. 2018, ApJ, 859, 11
Salim, S., Lee, J. C., Janowiecki, S., et al. 2016, ApJS, 227, 2
Salim, S., Rich, R. M., Charlot, S., et al. 2007, ApJS, 173, 267
Salmon, B., Papovich, C., Finkelstein, S. L., et al. 2015, ApJ, 799, 183
Salpeter, E. E. 1955, ApJ, 121, 161
Sánchez, S. F., Avila-Reese, V., Hernandez-Toledo, H., et al. 2018, RMxAA, 54, 217
Sánchez, S. F., Pérez, E., Sánchez-Blázquez, P., et al. 2016, RMxAA, 52, 171
Santini, P., Fontana, A., Castellano, M., et al. 2017, ApJ, 847, 76
Sargent, M. T., Béthermin, M., Daddi, E., & Elbaz, D. 2012, ApJL, 747, L31
Schreiber, C., Pannella, M., Elbaz, D., et al. 2015, A&A, 575, A74
Shin, K., Ly, C., Malkan, M. A., et al. 2020, MNRAS, staa3307, in press
Skibba, R. A., Engelbracht, C. W., Dale, D., et al. 2011, ApJ, 738, 89
Slavin, J. D., Dwek, E., Mac Low, M.-M., & Hill, A. S. 2020, arXiv:2009.01895
Speagle, J. S., Steinhardt, C. L., Capak, P. L., & Silverman, J. D. 2014, ApJS, 214, 15
Tacchella, S., Bose, S., Conroy, C., Eisenstein, D. J., & Johnson, B. D. 2018, ApJ, 868, 92
Tasca, L. A. M., Le Fèvre, O., Hathi, N. P., et al. 2015, A&A, 581, A54
Tomczak, A. R., Quadri, R. F., Tran, K.-V. H., et al. 2014, ApJ, 783, 85
Tomczak, A. R., Quadri, R. F., Tran, K.-V. H., et al. 2016, ApJ, 817, 118
van der Burg, R. F. J., Hildebrandt, H., & Erben, T. 2010, A&A, 523, A74
Weisz, D. R., Dolphin, A. E., Skillman, E. D., et al. 2014, ApJ, 789, 147
Whitaker, K. E., Franx, M., Leja, J., et al. 2014, ApJ, 795, 104
Whitaker, K. E., Pope, A., Cybulski, R., et al. 2017, ApJ, 850, 208
Whitaker, K. E., van Dokkum, P. G., Brammer, G., & Franx, M. 2012, ApJL, 754, L29
Williams, R. J., Quadri, R. F., Franx, M., van Dokkum, P., & Labbé, I. 2009, ApJ, 691, 1879
Wuyts, S., Labbé, I., Franx, M., et al. 2007, ApJ, 655, 51